J. Fluid Mech. (1998), *vol.* 367, *pp.* 107–137. Printed in the United Kingdom

On the determination of the onset of breaking for modulating surface gravity water waves

By MICHAEL L. BANNER AND XIN TIAN

School of Mathematics, The University of New South Wales, Sydney, NSW 2052, Australia

(Received 13 November 1996 and in revised form 13 February 1998)

Determining the onset of wave breaking in unforced nonlinear modulating surface gravity wave trains on the basis of a threshold variable has been an elusive problem for many decades. We have approached this problem through a detailed numerical study of the fully nonlinear two-dimensional inviscid problem on a periodic spatial domain. Two different modes of behaviour were observed for the evolution of a sufficiently steep wave group: either recurrence of the initial state or the rapid onset of breaking, each of these involving a significant deformation of the wave group geometry. For both of these modes, we determined the behaviour of dimensionless growth rates constructed from the rates of change of the local mean wave energy and momentum densities of the wave train, averaged over half a wavelength. These growth rates were computed for wave groups with three to ten carrier waves in the group and also for two modulations with seven carrier waves and three modulations with ten carrier waves. We also investigated the influence of a background vertical shear current.

Two major findings arose from our calculations. First, due to nonlinearity, the crest–trough asymmetry of the carrier wave shape causes the envelope maxima of these local mean wave energy and momentum densities to fluctuate on a fast time scale, resulting in a substantial dynamic range in their local relative growth rates. Secondly, a *universal* behaviour was found for these local relative growth rates that determines whether subsequent breaking will occur.

1. Introduction

Modulating wave groups and wave breaking are conspicuous features of the dominant waves on the open ocean, with a wide range of important consequences for fundamental geophysical processes as well as commercial maritime operations. Determining the onset of wave breaking in modulating wave groups of nonlinear surface gravity waves is a time-honoured problem that has been intensively studied both theoretically and observationally. Mathematically, it involves the local nonlinear stability of a free-surface flow with a large oscillatory basic state, for which no exact analytic theory at present exists.

The history of the problem has its origins in the steady, irrotational sharp-crested wave form of Stokes (1880) and Michell (1893). However, in the intrinsically unsteady circumstances in which breaking usually occurs, these steady limiting Stokes waves are probably never realized due to their inherent instability.

The papers of Benjamin & Feir (1967) and Zakharov (1968) are landmark studies in understanding the slowly varying evolution of weakly nonlinear wave groups. Yuen & Lake (1980) give an insightful overview of these studies and subsequent developments, involving both refinements to the analysis and observations of wave group evolution in wave tanks. Recent work in this area is reviewed by Hammack & Henderson (1993).

A very comprehensive account of the mathematical treatment of this topic was given by Yuen & Lake (1982) in terms of model equations for the evolution of the wave envelope. These equations are based on approximations to the exact equations of motion which are analytically intractable, and include the nonlinear Schrödinger equation (correct to third order in the wave steepness) and Dysthe's (1979) equation (correct to fourth order in the wave steepness). Underlying these approaches is the notion of a slowly varying wave train in which the (complex) envelope amplitude function varies slowly compared with the associated phase function. More recent papers extending the scope of such studies have been published by Lo & Mei (1984), Trulsen & Dysthe (1990) and Hara & Mei (1991), but these formulations still involve approximations to the full equations of motion which become questionable in the context of resolving fundamental issues on wave breaking. Major concerns are the limitations inherent in the assumptions of slow variation and the neglect of higher-order terms in the wave steepness parameter as the wave form steepens rapidly towards the onset of breaking.

Computations of the evolution to breaking of fully nonlinear, unsteady deep water waves were first reported by Longuet-Higgins & Cokelet (1976). Their results confirmed that unsteady breaking occurs at wave steepness levels well below that of the limiting steady configuration of the Stokes (1880) wave, with its sharp crests containing a 120° angle. Field observations are also inconsistent with the intuitive notion that the onset of breaking occurs at some critical wave geometry. For example, Holthuijsen & Herbers (1986) in their detailed study of wave breaking in the open ocean reported that it was difficult to distinguish the population of breaking waves from the overall wave population on the basis of their steepness probability distributions. A survey of such observational studies appears in the recent review article by Banner & Peregrine (1993). The degree to which observable details of unsteady wave breaking are reproduced by potential flow models is also discussed there (p. 382). The most recent study on this aspect is by Skyner (1996), who compared numerical predictions from Dold & Peregrine's (1986) code with internal velocity measurements made during the plunging process using particle image velocimetry (PIV) techniques. After a small shift of the numerical data to match the surface profiles, the predicted and measured kinematics were in close (within 2%) agreement. The predicted and measured surface shapes were also in very close agreement. From such studies, there can be little doubt that the essential features of two-dimensional wave breaking are captured by the Dold–Peregrine model well into the overturning regime, and that conclusions drawn from studying the model behaviour are likely to be relevant to the actual fluid dynamics underlying the onset of wave breaking in self-modulating wave groups. Clearly, final acceptance of any breaking criteria derived from numerical models must await experimental validation.

Other approaches addressing the onset of breaking have been through spectral decomposition and stability analyses. The detailed observational study of Melville (1982) largely confirmed the predictions of the two-dimensional Benjamin–Feir instability for initial carrier wave steepness levels up to 0.29. While the present study was restricted to moderate initial wave steepness, for steeper initial wave trains, Melville (1982) found that three-dimensional effects dominate the evolution. In a subsequent study, Melville (1983) investigated the modulational properties of these wave trains using Hilbert transform analysis and concluded that significant spatial modulation in the local wavenumber, frequency and envelope amplitude occurred within the evolving wave groups. A detailed analysis of the local crest stability by Longuet-Higgins & Cleaver (1994) and Longuet-Higgins, Cleaver & Fox (1994)

showed that the crest of a very steep irrotational gravity wave considered in isolation is unstable and quantified the growth rate in terms of the radius of curvature of the undisturbed crest. When related to the previously determined instability of the underlying steady wave (Tanaka 1983), this crest instability appeared to be coupled to the lowest superharmonic instability. These authors suggested that this crest instability should also be operative within modulating wave group situations, but this was not investigated in detail.

Other recent approaches have also contributed further knowledge and insight, particularly the contributions of Tulin & Li (1992), Wang, Yao & Tulin (1993) and Schultz, Huh & Griffin (1994). For a modulating wave group, Tulin & Li (1992) calculated the intra-wave depth-integrated energy differences for different subsections of a two-dimensional, second-order Stokes (1847) deep water wave train, consisting of the basic sinusoid plus its first harmonic, modulated according to the Benjamin–Feir sideband instability model. They examined the differences in the local depth-averaged energy along four subsections of length one half of the wavelength of the wave profile embracing the crest, trough, forward and rear faces of the wave. They concluded that significant differences in energy existed along the wave group, particularly between the trough region and crest regions of the steepest wave near the centre of the (symmetrical) wave group. Within the limitation of the second-order Stokes wave assumption, their study shows that such intra-wave energy imbalances are capable of increasing the energy flux to the forward face of a steep wave. This analysis did not establish an explicit criterion for the irreversible instability that leads to breaking, but highlighted the potential importance of intra-wave fluxes in this problem.

Wang *et al*. (1993) reported an interesting extension of previous approaches based on numerical solution of the fully nonlinear two-dimensional problem on a periodic domain, in which they synthesized a fully nonlinear numerical wave tank. Their simulations confirmed the ideas of Tulin & Li (1992) and suggested that a threshold for determining breaking onset involved the ratio of horizontal water speed at the crest to the group velocity. They found that for all cases that proceeded to breaking, this ratio exceeded one. However, even if this were shown to be valid generally, this quasi-kinematic criterion does not elucidate the underlying details of the instability. Also, as discussed below in §2.3.4, questions arise as to the definition of the group velocity in such nonlinear wave trains.

Schultz *et al*. (1994) used a fully nonlinear periodic-domain numerical code for irrotational flow to examine the relative merits of wave steepness and root mean square (r.m.s.) potential energy as breaking discriminants. They concluded that the r.m.s. potential energy computed over a local wavelength provides significantly less scatter for the various breaking scenarios they investigated. These include focused wave groups, straining by converging channel sidewalls, flow over obstacles and subharmonic instability. They also suggested an absolute criterion of potential energy/total wave energy exceeding 0.52. However, this kind of criterion does not appear to be valid in rotational flows, where the fraction potential energy/total wave energy has been shown to vary significantly as a function of the strength of the background vorticity (Teles da Silva & Peregrine 1988). Millinazzo & Saffman (1990) also reported significant changes to the wave shape and hence the potential energy in the presence of a surface shear layer. Therefore it is unlikely that a criterion involving a potential energy threshold can be valid universally. It is seen below that this kind of criterion also fails to explain the nature of the instability.

The results of these very recent studies have served to refocus attention on the problem and highlight the complex underlying issues involved in understanding what

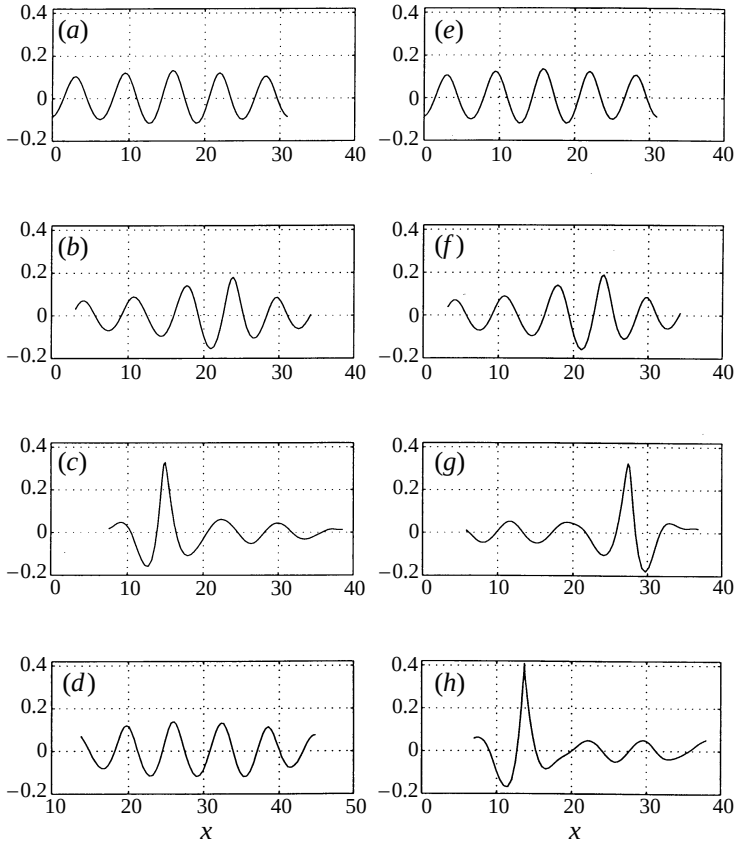

FIGURE 1. Free-surface profiles showing the two distinct evolution modes for an evolving wave group with five waves in the modulation, reproducing the results of DP. The wave propagation direction is from left to right. The initial group has a dominant centre frequency and two small spectral sidebands. The left-hand panels (*a*)–(*d*) have initial steepness $(ak)_0 = 0.11$ and show evolution with recurrence. The associated times in wave periods are (*a*) $t = 0$, (*b*) $t/2\pi = 40$, (*c*) $t/2\pi = 85$, (*d*) $t/2\pi = 165$. The right-hand panels (*e*)–(*h*) have $(ak)_0 = 0.1125$ and show evolution to breaking. The evolution times in wave periods are (*e*) $t = 0$, (*f*) $t/2\pi = 40$, (*g*) $t/2\pi = 70.1$, (*h*) $t/2\pi = 74.9$.

determines the onset of wave breaking and whether it is controlled by a universal threshold of some wave field parameter(s). The phenomenon is clearly illustrated by the computational wave example shown in figure 1, for which details of the underlying computational model are given below. Two deep water wave groups with five waves in one modulation are shown in the top panels (*a*) and (*e*) in this figure. Full details of the initial group structure are given below. They differ only marginally in the initial wave steepness $(ak)_0$ of the dominant spectral component, with the wave trains on the left- and right-hand panels having initial steepness 0.11 and 0.1125, respectively, so that the initial carrier waves are nonlinear. At similar intermediate times $t/2\pi = 40$, the two envelopes have deformed due to the nonlinear interactions within the group, resulting in a pronounced local growth of the wave envelope. At somewhat later times $t/2\pi = 85$ and 70.1 respectively, there has been further local growth of the dominant (largest-amplitude) section of the wave envelope, increasing the local energy and momentum densities. This is accompanied by a reduction in the envelope amplitude in other parts of the wave group, with a corresponding decrease in their local wave energy and momentum densities. It should be noted that the local steepness ak of the

largest carrier wave in the figure 1(*e–h*) is very similar to that in figure 1(*a–d*). Also, the r.m.s. potential energies of these two wave configurations are within a few percent of each other. The horizontal water velocities at the steep crests in these two configurations are respectively 0.94 and 0.70 of the *linear* group speed of carrier waves with this wavenumber and the Lagrangian vertical accelerations are very similar with crest values of -0.31.

During subsequent time steps, the steepest wave in panel (*c*) ceases to grow and then decreases in steepness as the wave train undergoes a recurrence towards the original configuration. In contrast, the steepest wave in panel (*g*), with a comparable steepness, subsequently amplifies rapidly and evolves to breaking. The evolution process produces significant spatial modulations not only in the local wave steepness, but also in the local propagation characteristics such as the wavenumber, frequency and phase speed of the carrier waves.

Modulating wave trains can be initiated in a variety of ways and the results of the study by Dold & Peregrine (1986, hereinafter referred to as DP) of a fully nonlinear, two-dimensional, periodic-domain free-surface computational model provided an appropriate starting point for the present study. In brief, they studied the evolution of wave groups composed of a fundamental carrier wave with small upper and lower sideband components, using as parameters the initial carrier wave steepness $(ak)_0$ and N, the number of waves in one modulational length. Their initial wave group had the structure of a uniform, finite-amplitude, steady deep-water wave train whose linear approximation is $\eta = a\cos x$. Scalings were used in the DP computational model, with $g = 1$ for the gravitational acceleration, $\rho = 1$ for the water density and a carrier wavelength of 2π. This gave unity as the reference values for the linear wavenumber, linear radian frequency and linear phase speed, with a corresponding wave period of $T = 2\pi$. On this primary wave are superimposed perturbations having the initial form

$$\epsilon a\cos\left(\frac{n+m}{n}x-\phi\right)+\epsilon a\cos\left(\frac{n-m}{n}x-\phi\right), \quad \text{with} \quad \epsilon = 0.1. \tag{1.1}$$

Here $N = n/m$, where n and m are integers that determine the initial perturbation wavenumbers. The calculations were limited to $3 \leqslant N \leqslant 10$ (see DP) with $3 \leqslant n \leqslant 10$ and $1 \leqslant m \leqslant 3$, providing sideband wavenumbers in the range [0.667, 1.333]. Also, following DP, the phase angle ϕ was usually taken as $\frac{1}{4}\pi$ and was chosen to give the most rapid growth.

The trend of the DP results is indicated in the lower part of figure 2. For a given N, breaking always occurs above the indicated initial steepness $[(ak)_0]$ threshold, and below it a recurrence occurs towards the original wave group. In contrast to the strong dependence of the evolution on the parameter space $\{N, (ak)_0\}$, the actual steepness at breaking $(ak)_{breaking}$ has no clear trend with N, as is seen in the upper part of figure 2. This conclusion is independent of the precise definition of the steepness at breaking, here taken to be the product of the local wavenumber and one-half of the elevation of the crest above the mean trough level.

The behaviour seen in figure 2 is among many fascinating aspects of this problem that motivated the present effort to understand what determines the evolution to breaking or to recurrence and whether this is controlled by a 'universal' threshold parameter. These fundamental issues are addressed in detail in the subsequent sections of this paper and are intended as a first step towards understanding the onset of breaking of the dominant waves at sea.

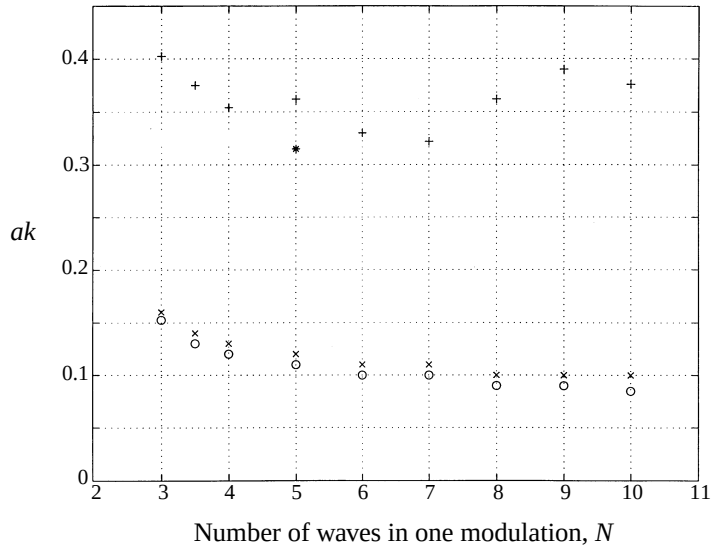

FIGURE 2. Carrier wave steepness for different values of N, the number of waves in one modulation. The lower set of points ○ and × are the initial steepness $(ak)_0$ for the recurrence and the breaking case with $\Omega = 0$ (zero background vorticity). This provides the boundary between these two modes, and reproduces the results of DP. The upper values indicated by + are the corresponding values at breaking $(ak)_{breaking}$ for $\Omega = 0$. The point ∗ shows $(ak)_{breaking}$ for $\Omega = 0.2$ for the case $N = 5$, highlighting the strong influence of the background shear on the steepness at breaking.

2. Methodology

2.1. *Overview*

Two-dimensional modulating wave groups with moderate initial steepness values have two distinct modes of evolution, as illustrated in figure 1. These sequences motivated the viewpoint pursued in this study: carrier waves in modulating nonlinear wave groups grow systematically only if there are sustained convergences of momentum flux and energy flux to a particular region of the group as it evolves. In the present conservative system, this must occur as an exchange process with other regions within the wave group undergoing a corresponding reduction in local energy and momentum density. We envisaged that carrier waves passing through the envelope maximum should proceed to break if the local mean wave momentum and energy densities have sufficiently large relative growth rates that persist for a sufficient duration. Otherwise, the envelope maximum may experience initial growth but then cease growing and evolve into a bounded behaviour such as the 'recurrence' mode seen in figure 1. Thus the basis of our approach to understand the onset of breaking was to calculate the behaviour of non-dimensional relative growth rates, following the wave group, of the local mean energy and momentum densities for different parts of the wave envelope.

In the absence of any suitable analysis techniques, we used a numerical approach. The DP free-surface code was used to calculate the evolution of the free surface of a modulating wave group. For any given time during the evolution, our interior code was used to compute the associated interior flow field from the free-surface configuration. This allowed us to investigate the detailed behaviour of the fundamental variables identified above for a range of initial wave group configurations.

In this context, the local mean is the spatial average taken over a suitable interval, such as the local wavelength L. While the choice of local averaging interval has a certain flexibility, it is important to note (see figure 1) that strong modulations occur

in the local wavelength L and these need to be taken into account. Details of the determination of the local wavenumber and related propagation characteristics are described below in §2.3.4. Local dimensionless relative growth rates may then be defined for the mean wave momentum density and energy density at each point along the wave train.

2.2. *Definitions*

2.2.1. *Fundamental variables*

The wavelength-averaged local mean wave momentum density $\hat{M}$ is defined as

$$\hat{M}(x,t) = L^{-1} \int_{x-L/2}^{x+L/2} \int_{-\infty}^{\eta} u(x',y',t)\,\mathrm{d}y'\,\mathrm{d}x'. \tag{2.1a}$$

The corresponding wavelength-averaged local mean wave energy density along the group $\hat{E}$ is defined by

$$\hat{E}(x,t) = L^{-1} \int_{x-L/2}^{x+L/2} \int_{-\infty}^{\eta} \tfrac{1}{2}(u^2+v^2)\,\mathrm{d}y' + \tfrac{1}{2}\eta^2 \;\mathrm{d}x'. \tag{2.1b}$$

Here x, y are the usual horizontal and vertical spatial coordinates, (u, v) is the corresponding velocity field, $y = \eta(x,t)$ is the free surface, $L(x,t)$ is the local wavelength, the waves are in deep water and the water density is taken as unity. The spatial averaging in (2.1) 'smears' the distribution of these mean quantities relative to the underlying carrier wave form. Other choices of average interval were found to provide much better localization of the envelopes of the mean momentum and energy densities and their growth rates. These were based on half-wavelength averages, in which L is replaced by $L/2$ in the definitions (2.1). These key averages, denoted by $\hat{M}_{1/2}$ and $\hat{E}_{1/2}$ respectively, formed the basis of this study.

2.2.2. *Relative growth rates*

Dimensionless growth rates $\beta_M(x,t)$ and $\beta_E(x,t)$ were then constructed for the relative rates of change of these locally averaged quantities, with subscripts suppressed, as follows:

$$\beta_E = \frac{1}{\omega\hat{E}}\frac{\mathrm{D}_*\hat{E}}{\mathrm{D}t} \tag{2.2a}$$

and

$$\beta_M = \frac{1}{\omega\hat{M}}\frac{\mathrm{D}_*\hat{M}}{\mathrm{D}t} = \frac{1}{\omega\hat{M}^2}\;\hat{M}\frac{\mathrm{D}_*\hat{M}}{\mathrm{D}t}\;. \tag{2.2b}$$

In these growth rate expressions, $\mathrm{D}_*/\mathrm{D}t = \partial/\partial t + c_{\langle E \text{ or } M\rangle}\,\partial/\partial x$ is the derivative following the envelope of $\hat{E}(x,t)$ or $\hat{M}(x,t)$. A detailed discussion of the envelope propagation speeds $c_{\langle E \text{ or } M\rangle}$ is given below in §2.3.4. Also, as discussed in detail in §2.3.4, the local frequency ω was found to vary along the wave group by up to a maximum of 25%, but for the purpose of determining a breaking threshold, it was more convenient to normalize by the linear carrier wave frequency.

For small-slope spatially uniform gravity wave trains, $\hat{E}$ and $\hat{M}$ in (2.1*a*, *b*) have constant values, of second order in the wave steepness (see Phillips 1977, §3.2). For the unsteady highly nonlinear wave groups in this study, $\hat{E}$ and $\hat{M}$ are still small quantities but are spatially non-uniform due to the strong local modulations that occur. $\hat{M}$ can be positive, or negative (the local mean momentum can be opposite to the propagation direction) or zero, while $\hat{M}_{1/2}$ ranges over larger values. As these quantities appear in the denominators of the relative growth rate expressions, they can locally become

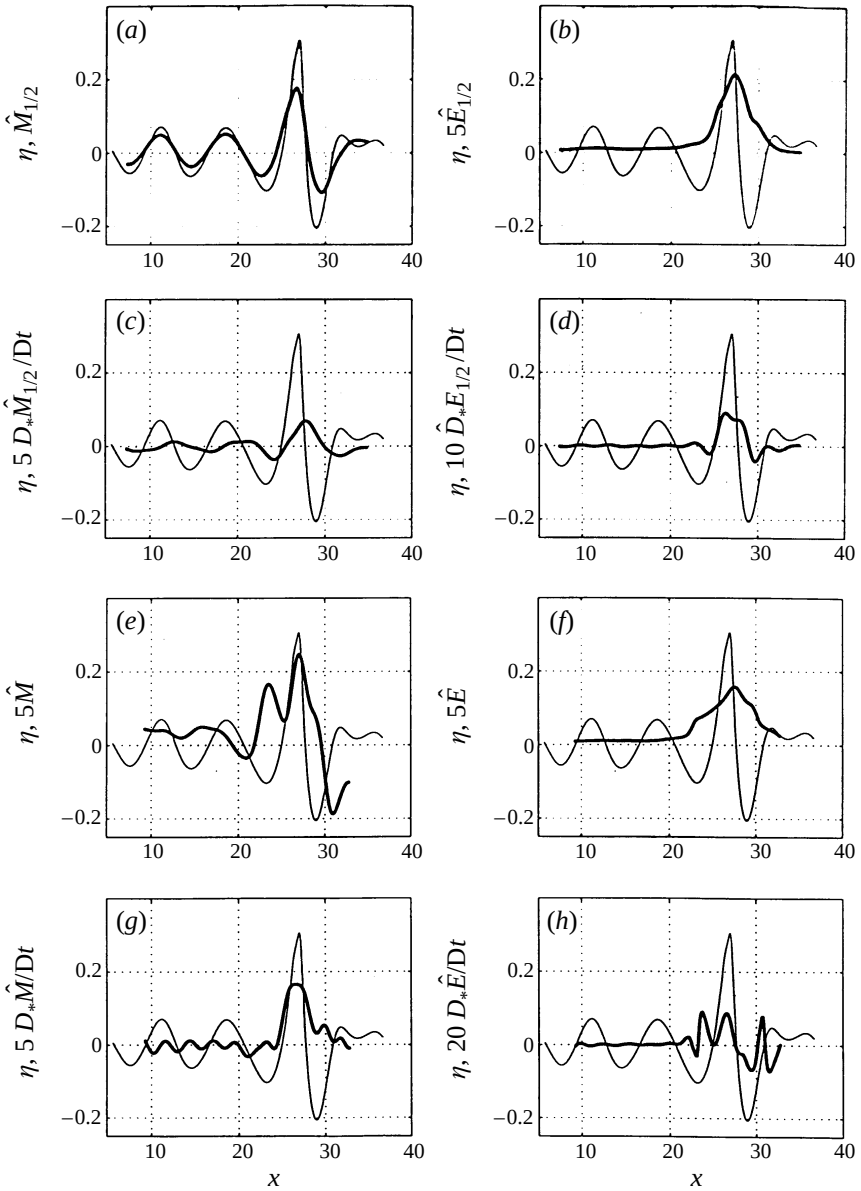

FIGURE 3. Typical distributions along the wave group of $\hat{E}$, $\hat{M}$, $\hat{E}_{1/2}$ and $\hat{M}_{1/2}$ and their $\mathrm{D}_*/\mathrm{D}t$ derivatives for $\Omega = 0$, $(ak)_0 = 0.12$, $N = 5$ at $t/2\pi = 60$ for the initial wave group (1.1). Each panel shows the wave elevation $y = \eta$ (thin line) and the corresponding density or $\mathrm{D}_*/\mathrm{D}t$ distributions. (*a*) $\hat{M}_{1/2}$, (*b*) $5\hat{E}_{1/2}$, (*c*) $5\mathrm{D}_*\hat{M}_{1/2}/\mathrm{D}t$, (*d*) $10\mathrm{D}_*\hat{E}_{1/2}/\mathrm{D}t$, (*e*) $5\hat{M}$, (*f*) $5\hat{E}$, (*g*) $5\mathrm{D}_*\hat{M}/\mathrm{D}t$, (*h*) $20\mathrm{D}_*\hat{E}/\mathrm{D}t$. Note the poor localization of $\mathrm{D}_*\hat{E}/\mathrm{D}t$ in (*h*).

vanishingly small and give rise to spurious large local values of $\beta_E(x, t)$ and $\beta_M(x, t)$ that are not relevant to the issue of wave breaking. These were avoided by imposing a lower threshold for their magnitudes. Validation of this procedure is detailed in §2.3.3.

Anticipating results for which the techniques are described subsequently, figures 3(*a*)–3(*h*) show a set of typical distributions of $\hat{E}$, $\hat{M}$, $\hat{E}_{1/2}$ and $\hat{M}_{1/2}$ and their $\mathrm{D}_*/\mathrm{D}t$ derivatives (after thresholding) for a wave group configuration where the wave group

has evolved significantly from its initial symmetric configuration and is in the process of growing locally towards breaking. These figures show the oscillatory spatial character of the mean momentum density distribution as well as the degree of localization of the rates of change for the various averages. It is evident that $\mathrm{D}_* E/\mathrm{D}t$ is not well localized along the envelope of $\hat{E}$ and was considered unsuitable for the present purposes. Also, while $\mathrm{D}_* M/\mathrm{D}t$ is well-localized, the envelope of $\hat{M}$ often developed multiple local peaks due to the oscillatory character of $\hat{M}$, as may be seen in figure 9. The relative amplitudes of these local peaks can fluctuate on a fast time scale during the evolution, making it difficult to identify a quasi-steadily progressing envelope maximum at which to identify the corresponding value of $\beta_M(x, t)$. Hence we limited our investigation to the behaviour of the half-wavelength mean energy and momentum densities, as each of these quantities provided well-localized relative growth rates and well-defined stable envelope maxima where the corresponding growth rate could be evaluated.

2.3. *Computational and numerical techniques*

2.3.1. *Free-surface code*

The fully nonlinear two-dimensional inviscid free-surface code used in this study was developed by DP and is documented fully by Dold (1992). It uses the boundary element method and is capable of representing the wave profile past the point of overturning. We note that this code can also compute wave group evolution with a uniform background vorticity. This allowed us to examine the influence of surface shear currents on wave breaking and to extend the scope for examining the 'universality' of any prospective breaking criterion.

We carefully checked the performance of this code for the influence of various kinds of numerical instabilities as discussed comprehensively by Dold (1992, pp. 101–109). He identified several possible types of numerical instability that can arise in the solutions, including weak, strong and steep-wave instabilities, and provided a comprehensive discussion of these numerical instabilities and their suppression. Briefly, strong instability was eliminated by using a small precision control parameter ϵ. Weak instability was eliminated by selecting a sufficiently large order l_B for backward differencing. Steep-wave instability was suppressed in our calculations by using sufficiently small ϵ, fifth-order backward differencing and sufficiently large NP (number of points/wave), as well as smoothing.

In our calculations, the choice of $\epsilon = 0.001$, $l_B = 5$ and $NP = 16$ avoided these numerical instabilities. We verified that there was no significant effect of numerical instability on our results as follows.

(i) We compared the results obtained with and without the use of smoothing and found no significant difference. The appearance of strong numerical instability was controlled even without smoothing in our case of non-forced waves with initial steepness $(ak)_0$ smaller than 0.16.

(ii) We used various values of ϵ in test cases and it was found that $\epsilon = 0.001$ was sufficiently small to obtain a stable solution.

(iii) We tested various values of NP and it was found that $NP = 16$ was sufficiently large to ensure a stable result.

(iv) We used various values of l_B for some typical examples and as suggested by Dold (1992), it was found the choice of $l_B = 5$ improved the time-stepping accuracy.

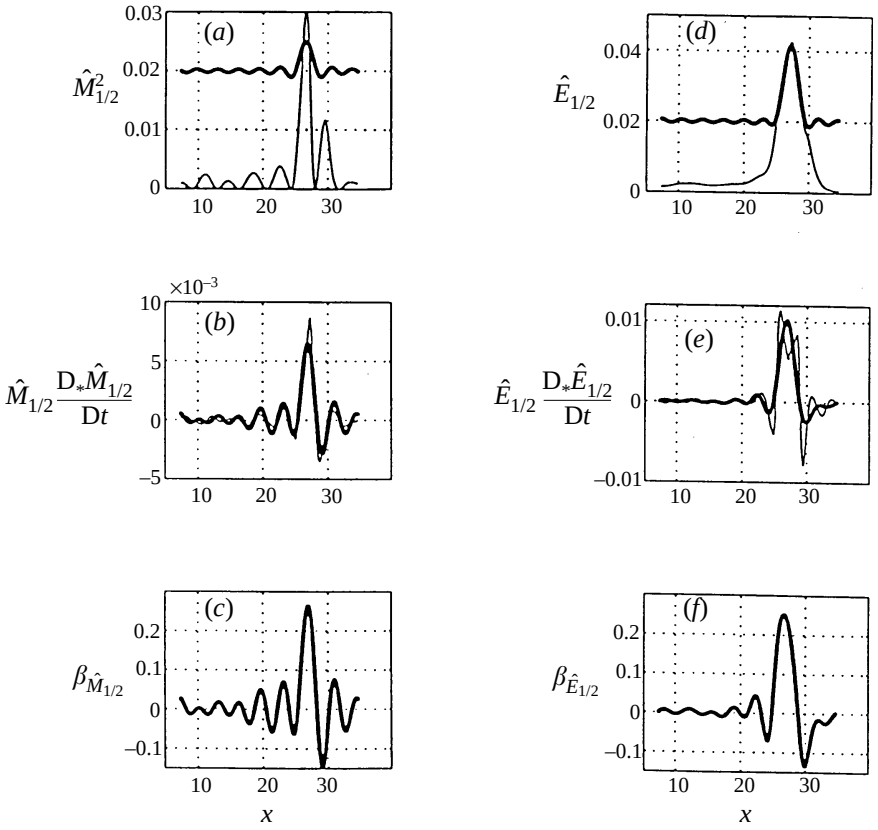

FIGURE 4. Typical distributions of the numerator and denominator terms in the relative growth rates ((2.2*a*) and (2.2*b*)) showing the effects of low-pass filtering and thresholding using the levels $\epsilon_M = \epsilon_E = 0.02$ for $L = 1/2$. The thin and thick lines show each distribution before and after low-pass filtering and thresholding, respectively. The wave conditions are as specified in figure 3.

2.3.2. *Interior velocity field code*

The calculation of $\beta(x, t)$ in (2.2) requires detailed knowledge of the interior flow field in the computational domain. Most of the cases investigated were of irrotational flow, which is fully determined by the instantaneous boundary configuration as a consequence of Cauchy's integral theorem. The details are given in Appendix A. The influence of a uniform background vorticity was also investigated using the DP code, as for this case it is possible to decompose the motion into the superposition of a potential flow and a uniform shear flow.

It proved to be computationally efficient to use the hybrid approach of calculating the surface profiles and interior flows successively. The horizontal resolution of the DP code output, was typically 16 points per wave. Our interior flow code was based on the spectral method and produced a much higher resolution. We used spline interpolation of the free-surface code output, typically using between 768 and 1024 points horizontally over the computational interval. Also, the depth of this domain was always more than eight times the carrier wavelength, ensuring deep water conditions. Overall, this approach provided an efficient and accurate interpolation of the interior flow field beneath the waves.

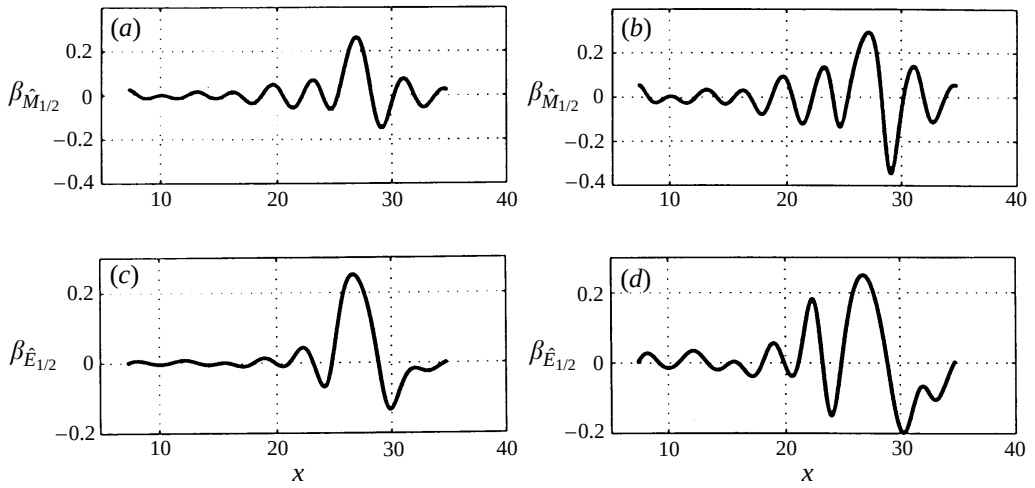

FIGURE 5. Distributions of β along the wave profile showing the insensitivity of β^{max} to the choice of threshold for $\hat{M}_{1/2}$: (*a*) $\epsilon_M = 0.02$, (*b*) $\epsilon_M = 0.005$; and $\hat{E}_{1/2}$: (*c*) $\epsilon_E = 0.02$, (*d*) $\epsilon_E = 0.005$.

2.3.3. *Thresholding*

As pointed out above, the local mean momentum and energy densities along the wave group can become arbitrarily small and generate local singularities in the relative growth rates. These were suppressed by applying lower bound thresholds as follows: if $|\hat{M}| \leqslant \hat{M}_{min}$ then $|\hat{M}| = \hat{M}_{min}$ and similarly for $\hat{E}$. Clearly, the choice of threshold should only affect $\beta_M(x,t)$ or $\beta_E(x,t)$ at isolated locations and should only serve to reject large relative growths caused by vanishingly small denominator terms. The physically relevant growth rates of the envelope maxima were not affected by this process. Typical choices for such thresholding were $\epsilon_m = \epsilon_e = 0.02$ for $L = 1/2$ and $\epsilon_m = 0.003$ for $L = 1$. Figure 4 shows the influence of thresholding and low-pass filtering (see §2.4) in the numerator and denominator of the growth rate expressions (2.2). Figure 5 shows the insensitivity of the choice of threshold to the determination of the resultant maximum growth rates.

2.3.4. *Propagation characteristics*

Local wavenumber. Because of the significant modulations in the local carrier wavelength that arise during the evolution of the wave group, throughout this study the local wavelength $L(x,t)$ was obtained from $2\pi/k(x,t)$, where $k(x,t)$ is the local wavenumber along the wave profile at time t; $k(x,t)$ was calculated systematically from the derivative $\partial\phi/\partial x$ of the unfolded phase function $\phi(x,t)$ computed from the Hilbert transform of the free-surface profile. Some post-filtering was sometimes necessary to eliminate spurious wavenumber results that arose where the local conditions for applying the Hilbert transform were not ideal. This was required at steep crests, which are very much sharper than the adjacent troughs, and also where a significantly shorter local wavelength disturbance appeared on the profile above or below the mean level. Low-pass filtering was carried out by removing an appropriate number of high-wavenumber Fourier components determined by our need for an accurate representation of the local wavelength. Extensive testing indicated that even for extreme waves just prior to breaking, the calculated wavelengths after filtering were within $\pm 5\%$ of the actual physical wavelength determined from the wave profile. Figure 6

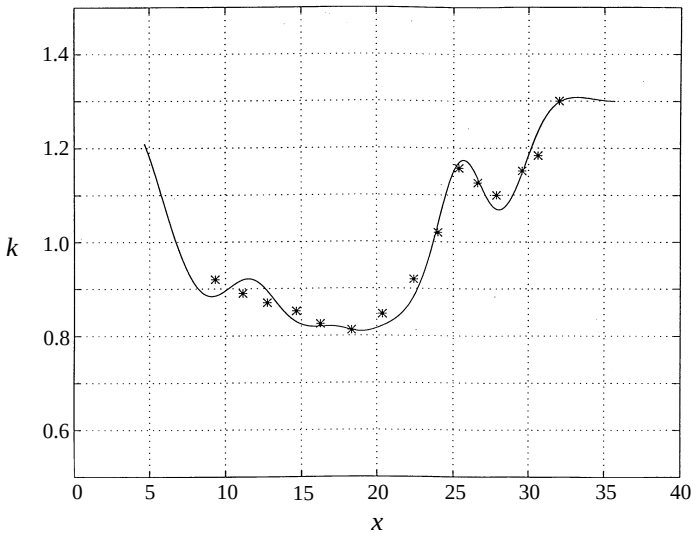

FIGURE 6. Comparison of computed wavenumber distribution (continuous line) and local wavenumbers estimated from direct measurement of crests, troughs and zero-crossings for the case of $\Omega = 0$, $N = 5$ and $(ak)_0 = 0.12$ at $t/2\pi = 50$.

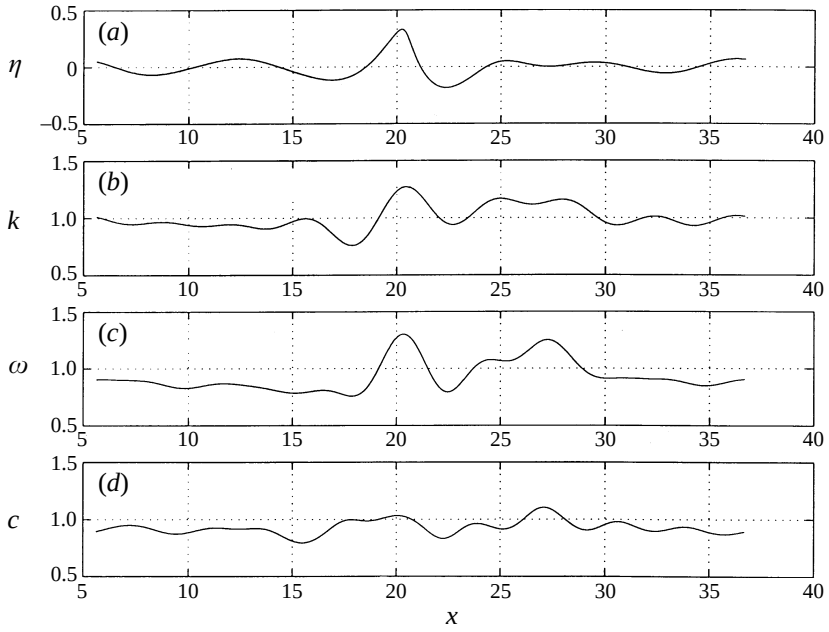

FIGURE 7. Horizontal distribution of propagation characteristics just prior to the commencement of recurrence at $t/2\pi = 84.4$ for the case shown in figure 1: (*a*) wave elevation profile, (*b*) local wavenumber k, (*c*) local frequency ω, (*d*) local phase speed c.

shows the accuracy of such a wavenumber determination just prior to breaking. Figures 7(*b*) and 8(*b*) show typical wavenumber distributions along the modulating nonlinear wave group. This approach was preferred to wavelet analysis as it gave better accuracy in test cases such as shown in figure 6.

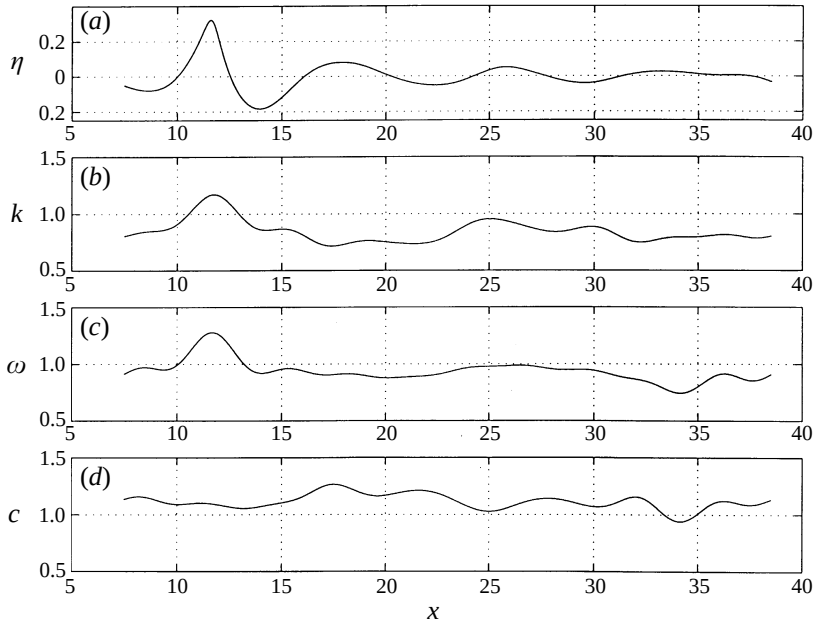

FIGURE 8. Horizontal distribution of propagation characteristics just prior to the commencement of breaking at $t/2\pi = 58$ for $(ak)_0 = 0.12$: (*a*) wave elevation profile, (*b*) local wavenumber k, (*c*) local frequency ω, (*d*) local phase speed c.

Local frequency. This was also computed from the time derivative $-\partial\phi/\partial t$ of the phase function of the elevation (or of the steepness) at closely separated times, using $\omega \approx -(\phi(t+\Delta t)-\phi(t-\Delta t))/2\Delta t$. This also required low-pass filtering to match the frequency as determined at selected phase points on the wave. Typical distributions of ω along the wave profile are shown in figures 7(*c*) and 8(*c*).

Local phase speed. This is the local frequency divided by the local wavenumber and is shown plotted in figures 7(*d*) and 8(*d*).

Envelope propagation speed for local mean energy and momentum densities. For a linear wave group, the computation should produce energy and momentum envelope speeds $c_{\langle E\rangle}$, $c_{\langle M\rangle}$ equal to the familiar group velocity $c_g = 0.5$. We validated our computational approach for the following specific case by calculating the envelope velocities of these quantities for a linear wave group of the form

$$\eta = 0.01\cos(x) + 0.005\cos(1.2x - \pi/18)$$

for incremental time steps of 0.2. The envelope of $\hat{E}$ was obtained directly as this quantity is positive definite, but that of $\hat{M}$ required a Hilbert transform envelope calculation. The determination of $c_{\langle E\rangle}$ and $c_{\langle M\rangle}$ at time t followed by calculating the mean horizontal displacement of the respective envelopes in the interval $[t-\Delta t, t+\Delta t]$, and dividing by the time increment $2\Delta t$. The resulting average values of $c_{\langle E\rangle}$ were very close to 0.5. The corresponding calculation for $c_{\langle M\rangle}$ was less straightforward due to computational noise at such low wave steepness levels and was not pursued.

For the nonlinear wave groups in this study, it is interesting to recall the discussion by Peregrine & Thomas (1979) on the formal extension of the group velocity concept to nonlinear waves. From their discussion, there is no unique definition of the group velocity, and the most appropriate choice is not clear for cases where strong amplitude and wavenumber modulations occur. To circumvent these conceptual difficulties, we

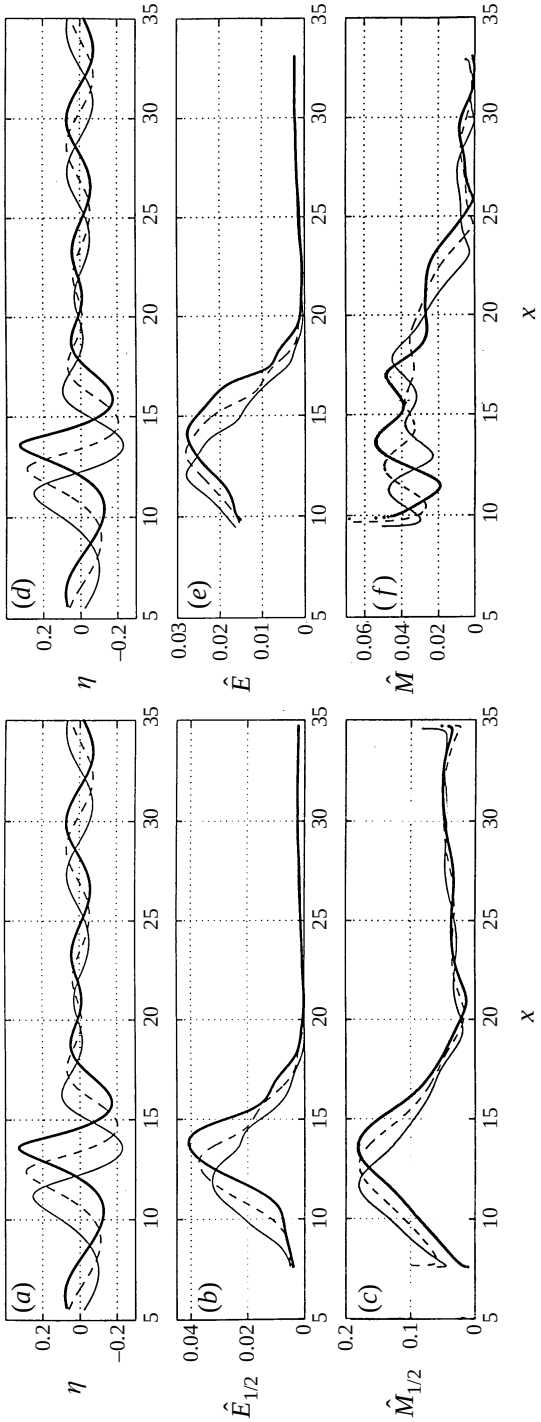

FIGURE 9. Details of the envelope propagation for the local mean momentum and energy densities for the breaking wave case with $(ak)_0 = 0.12$ at $t/2\pi = 55.8$ (——), 56 (– – – – –) and 56.2 (—·—). (*a*) Elevation profile, (*b*) envelope of $\hat{M}_{1.2}$, (*c*) envelope of $\hat{E}_{1/2}$, (*d*) elevation profile, (*e*) envelope of $\hat{M}$, (*f*) envelope of $\hat{E}$.

simply used the envelope propagation speeds $c_{\langle E\rangle}$ and $c_{\langle M\rangle}$ as the relevant propagation velocities, determined by the same finite difference approach as described above. With the local unsteady deformation of these envelopes entering as an additional consideration, we were limited to calculating the envelope speed by analysing the motion of the envelope at its maximum. Figure 9 illustrates the situation for $\hat{E}_{1/2}$ and $\hat{M}_{1/2}$ for three incremental time steps at a strongly evolving stage of a wave group with initial steepness 0.12. This figure also shows the envelope evolution for $\hat{E}$ and $\hat{M}$. As discussed in §2.2, the multiple local peaks of $\hat{M}$, seen clearly in this figure, were responsible for our decision not to retain $\hat{M}$ as a primary dynamical variable. Even then, the envelope motion analysis for $\hat{M}$ showed that the envelope speeds were measurably less than the phase speed of the individual carrier waves. The results obtained for $c_{\langle E\rangle}$ and $c_{\langle M\rangle}$ are discussed in §3.2.1.

2.4. *Growth rate computations*

The growth rate computations for $\beta_E(x,t)$ and $\beta_M(x,t)$ defined in (2.2*a*) and (2.2*b*) require calculating $\mathrm{D}_*/\mathrm{D}t = \partial/\partial t + c_{\langle E \text{ or } M\rangle}\partial/\partial x$ of the local average energy and momentum densities, normalizing by the local value of these quantities and by the *local* frequency ω. The latter involves the laborious calculation of $\omega(x,t)$ throughout the evolution. To avoid this, we decided to retain the linear carrier wave frequency $\omega = 1$ in the relative growth rate expressions. When rescaled by the true local frequency at the envelope maxima, the actual maximum relative growth rate is reduced typically by a similar factor of around 25% for both breaking and recurrence cases. For convenience in establishing a breaking threshold, we decided to retain the linear frequency as the reference normalizing frequency in the relative growth rate expressions throughout this paper.

In calculating the temporal growth rate contribution, an approximation described in Appendix B was used that reduced the computational effort appreciably. This approximation was used only after it was established that the errors involved were not significant. Finally, we point out that the β-distributions required low-pass filtering to obtain suitably smooth curves from which to extract β^{max}. However, by varying the number of Fourier modes retained in each case, we checked very carefully that the filtering did not influence the results for β^{max}.

3. Results

3.1. *Linear case*

As a familiar test case, we examined an infinitesimal-slope wave group formed by the linear superposition of two slightly different-wavelength equal-amplitude infinitesimal-slope wave trains with $(ak)_0 \sim 0.01$. Here, the resulting wave group envelope is sinusoidal, with a corresponding sinusoidal distribution of $\hat{E}$ and $\hat{M}$. Individual carrier waves, whose phase speed is twice the group speed, move through the group and are modulated accordingly, with a given carrier wave experiencing a growth and decay cycle as it passes through the group. The main point is that when travelling with the linear *group velocity* ($c_{\langle E\rangle} \approx c_{\langle M\rangle} \approx 0.5$), the rates of change of $\hat{E}$ and $\hat{M}$ are zero at any location within the group pattern, and hence the growth rates $\beta_E(x,t)$ and $\beta_M(x,t)$ are also zero everywhere within the group. Our computations successfully reproduced this behaviour.

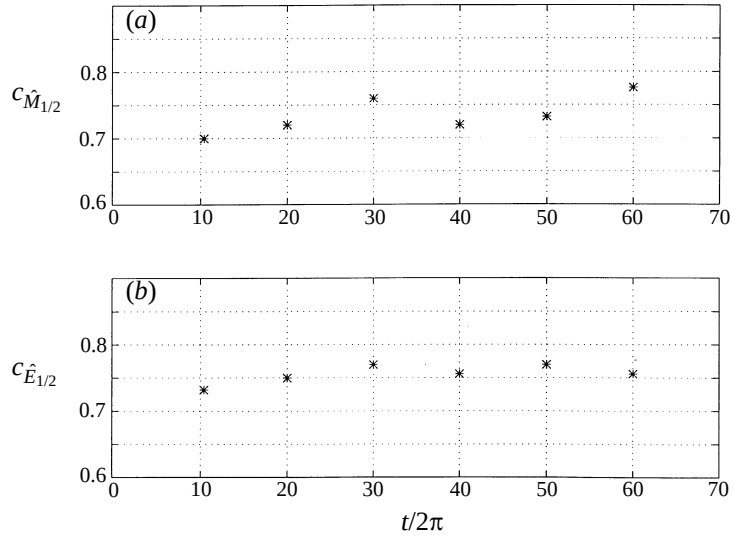

FIGURE 10. Envelope propagation speeds for the peak of the envelope at different times for the breaking wave case with $(ak)_0 = 0.12$ for (*a*) $\hat{M}_{1/2}$ and (*b*) $\hat{E}_{1/2}$.

3.2. *Fully nonlinear modulating wave trains*

3.2.1. *Envelope propagation speeds*

Propagation speeds of the energy maxima for $\hat{E}_{1/2}$ and $\hat{M}_{1/2}$ were estimated for different stages of evolution of the nonlinear wave groups, both recurrent and breaking. The end result was that the behaviour was consistently represented by taking $c_{\langle E\rangle} \approx c_{\langle M\rangle} \approx 0.75$ for both densities. A typical example is shown in figure 10. This is consistent with the observations of Melville (1983, §5) and the envelope speed of the wave packet shown in figure 6 of Rapp & Melville (1990). The error incurred subsequently by taking this value as constant throughout the evolution was not significant in assessing the maximum value of the dimensionless growth rates. This was checked by calculating the effect of different $c_{\langle E\rangle}$ and $c_{\langle M\rangle}$ values on $\mathrm{D}_* \hat{E}_{1/2}/\mathrm{D}t$ and $\mathrm{D}_* \hat{M}_{1/2}/\mathrm{D}t$. The choice of values of 0.6 and 0.9 naturally changes the relative speeds of the growth rate distributions with respect to the envelope, but this was found to have negligible impact on the maximum values of these growth rates.

3.2.2. *Localization of the rates of change of $\hat{E}_{1/2}$ and $\hat{M}_{1/2}$*

In figure 3 it was seen that the local behaviour of $\hat{E}_{1/2}$ and $\hat{M}_{1/2}$ and their $\mathrm{D}_*/\mathrm{D}t$ derivatives provided a basis for investigating the underlying dynamics and energetics. However, it is the relative growth rates at the envelope maxima of $\hat{E}_{1/2}$ and $\hat{M}_{1/2}$ expressed through the corresponding dimensionless growth rates defined in (2.2) that should determine the threshold for breaking.

This phase of the investigation led to new insights into the underlying processes leading to recurrence or breaking. These are visualized through the typical case of $N = 5$ shown in figure 1 and are described as follows.

(*a*) Except very close to the onset of breaking (which is described in (*c*) below), the envelope maxima of $\hat{E}_{1/2}$ and $\hat{M}_{1/2}$ fluctuate significantly on a fast time scale of $O(2T)$. This arises from the half-wavelength averaging in combination with the asymmetric carrier wave form shape due to nonlinearity, and necessitated examining the detailed behaviour of the modulating wave train with a much higher temporal solution than has

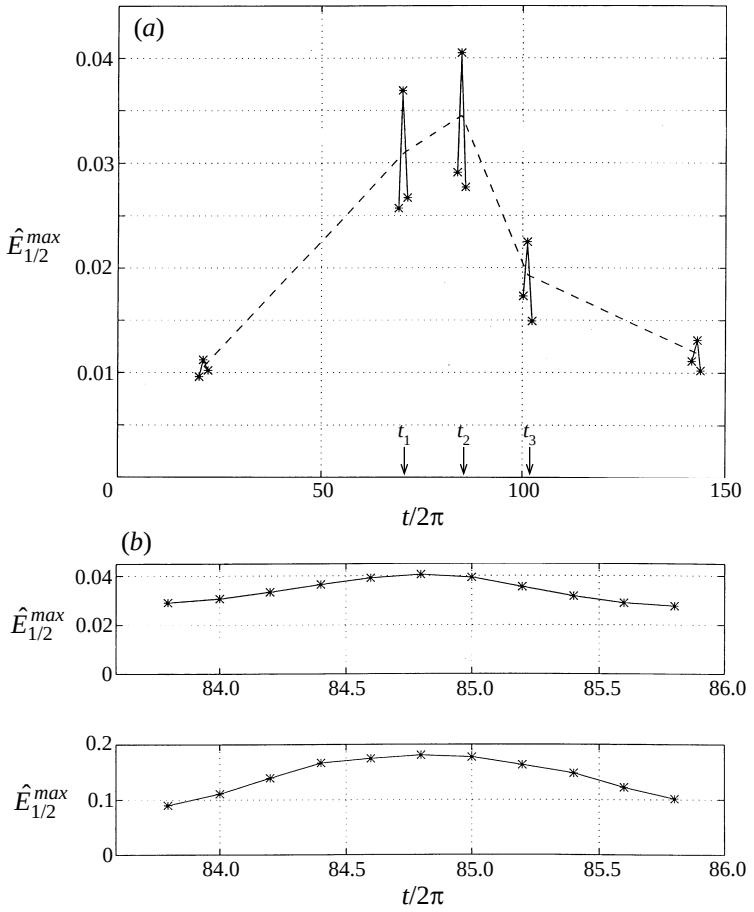

FIGURE 11. (*a*) The dashed line shows the evolution of the trend of the mean value of $\hat{E}_{1/2}^{max}$ averaged over several wave periods for the entire recurrence cycle shown in figure 1. The solid line segments terminating in $*$ show the extent of the local fluctuations of the envelope maxima of $\hat{E}_{1/2}$ at several different times during the entire recurrence cycle shown in figure 1. The indicated times t_1, t_2 and t_3 occur during the growth, peak and decay phases respectively. (*b*) The local behaviour at the peak of the recurrence cycle in $t/2\pi \in (83.8, 85.8)$ of the envelope maxima of $\hat{E}_{1/2}$ and $\hat{M}_{1/2}$ over an expanded time scale at the peak of the recurrence cycle.

been reported previously. These fluctuations are discussed in greater detail in Appendix C. Figure 11 illustrates the strength of these fluctuations in the local densities for the case $N = 5$ shown in figure 1. Figure 11(*a*) shows the significant level of the local variation in $\hat{E}_{1/2}$ at representative times within the growth and recurrence cycle. The other local mean densities fluctuate similarly, as seen in figure 11(*b*) which expands the temporal resolution of their behaviour in the short time interval $t/2\pi \in [83.8, 85.8]$ at the peak of the recurrence cycle. These fluctuations also occur in the envelope maximum of the surface elevation, as discussed below in (*b*).

(*b*) For the typical recurrence case of figure 1, figure 12 shows how the relative dimensionless growth rate distributions $\beta_{\langle E \text{ or } M \rangle}$ evolve relative to the maxima of the envelopes of $\hat{E}_{1/2}$ and $\hat{M}_{1/2}$. Due to their propagation speed exceeding the envelope speeds $c_{\langle E \text{ or } M \rangle}$, the $\beta_{\langle E \text{ or } M \rangle}$ fluctuate rapidly at the envelope maxima of $\hat{E}_{1/2}$ and $\hat{M}_{1/2}$. These growth rates *at the envelope maxima* are central to the discussion and are designated $\beta_{\langle E \text{ or } M \rangle}^{max}$. Travelling with the envelope speed, it is seen that the $\beta_{\langle E \text{ or } M \rangle}^{max}$

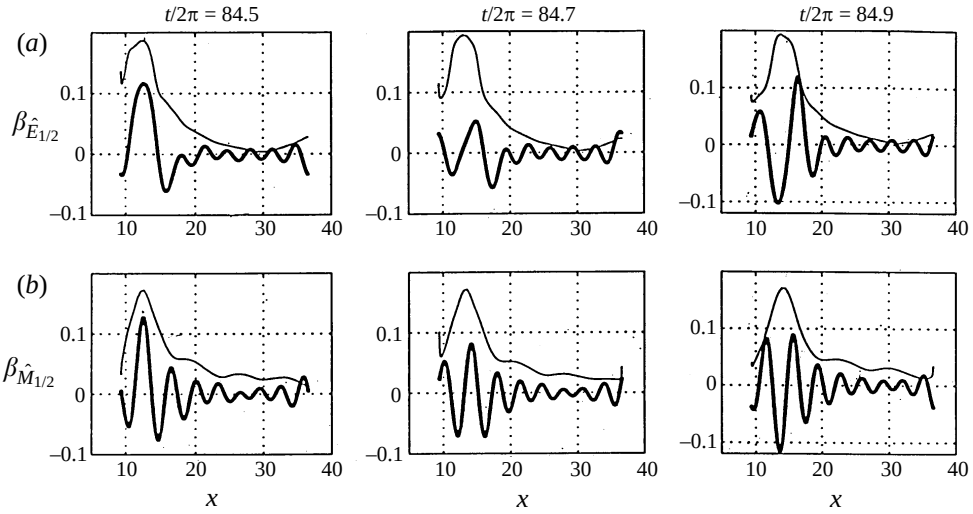

FIGURE 12. A typical example of the localization of the relative growth rates β of (*a*) $\hat{E}_{1/2}$ and (*b*) $\hat{M}_{1/2}$ along the wave envelope, shown as thick lines for the recurrence case of figure 1 at the three times $t/2\pi = 84.5$, 84.7 and 84.9. The thin line in each figure is the envelope of the corresponding mean energy or momentum density. Note how the growth rates change in time from positive through zero to negative at the envelope maxima.

undergo variations many times the local average value over a time scale of $O(2T)$. This is superimposed on a much slower mean growth or decay.

Figure 13 shows this key property of the $\beta^{max}_{\langle E \text{ or } M \rangle}$ at three different times t_1, t_2 and t_3 during the recurrence cycle indicated in figure 11(*a*). From these plots it is seen that the long-term mean growth rate is positive, nearly zero and negative respectively at these three times. The fast variation of the growth rate is clearly associated with the $O(2T)$-period fluctuations of the maximum of the wave elevation envelope discussed in (*a*). Correspondingly, for each of the $\beta^{max}_{\langle E \text{ or } M \rangle}$ there is a maximum growth rate over a local time interval of $O(2T)$, designated $\beta^{lmax}_{\langle E \text{ or } M \rangle}$. In this recurrence case, it is seen that $\beta^{lmax}_{\langle E \text{ or } M \rangle}$ attains a maximum of 0.2 for both $\hat{E}_{1/2}$ and $\hat{M}_{1/2}$. This behaviour of $\beta^{lmax}_{\langle E \text{ or } M \rangle}$ contrasts strongly with the case that proceeds to breaking in figure 1, discussed below in (*c*).

(*c*) Once $\beta^{lmax}_{\langle E \text{ or } M \rangle}$ reaches the recurrence maximum of 0.2, figure 14 shows how the growth rate distributions $\beta_{\langle E \text{ or } M \rangle}$ almost 'phase-lock' to the envelope maximum during the ensuing $O(0.5T)$ interval just before breaking. As seen in figure 15, this results in the envelope maxima of $\hat{E}_{1/2}$ and $\hat{M}_{1/2}$ now experiencing sustained $\beta^{max}_{\langle E \text{ or } M \rangle}$ levels of $O(0.2)$ during this time interval. Only minor variations of this behaviour were found for each of the other breaking onset cases we examined.

Figure 16 shows the entire time evolution for both recurrence and breaking cases of the respective $\beta^{lmax}_{\langle E \text{ or } M \rangle}$ for $\hat{E}_{1/2}$ and $\hat{M}_{1/2}$ for the case $N = 5$ corresponding to figure 1. Also shown is the case of a slightly steeper initial wave group with $(ak)_0 = 0.12$. This case proceeds to break earlier than for $(ak)_0 = 0.1125$, with a higher maximum growth rate occurring during the final approach to breaking.

3.2.3. *General determination of breaking or recurrence*

Overall, we found that the onset of recurrence or breaking was determined by the behaviour of $\beta^{lmax}_{\langle E \text{ or } M \rangle}$ during the evolution of the wave group. Obtaining the behaviour of the short-term maximum growth rates $\beta^{lmax}_{\langle E \text{ or } M \rangle}$ required an extensive searching

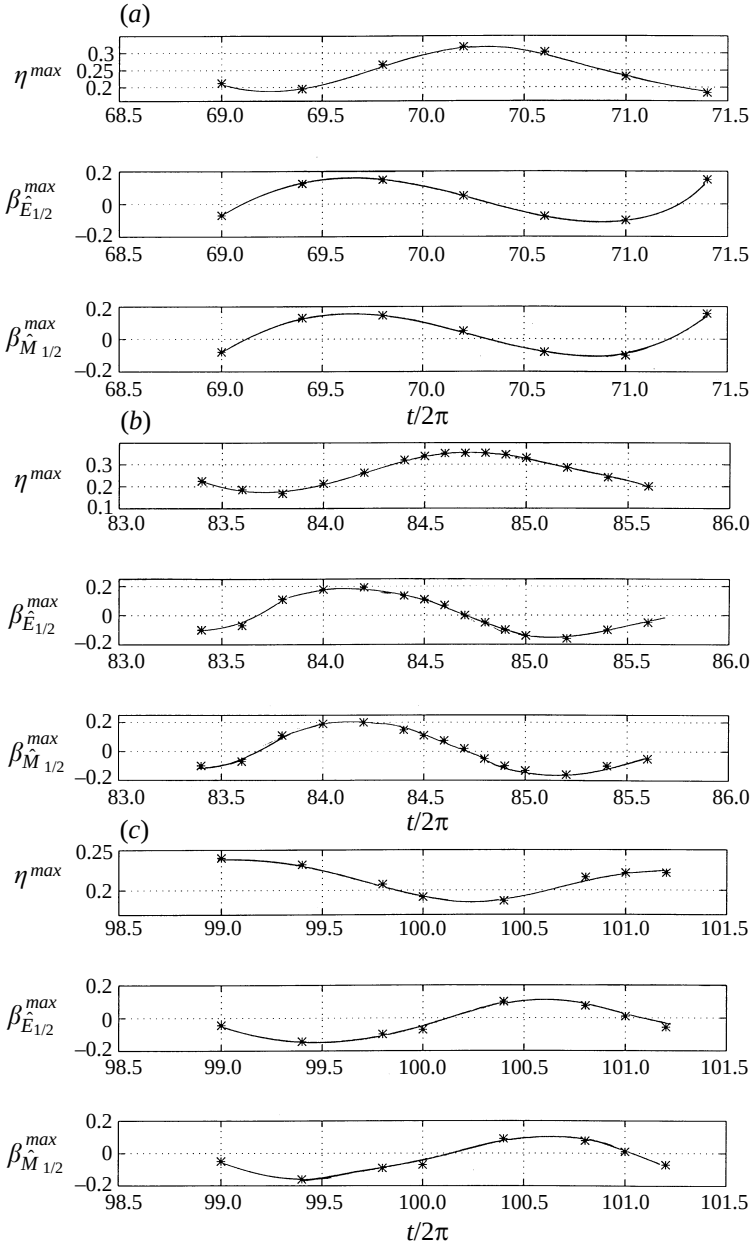

FIGURE 13. The local fluctuations of η^{max}, the maximum of the surface elevation envelope in relation to β^{max} for $\hat{E}_{1/2}$ and $\hat{M}_{1/2}$ at three stages t_1, t_2 and t_3 during the evolution of the recurrence case of figure 1 and coinciding with the times in figure 1 during which the local *mean* growth rate is positive, zero and negative respectively. (*a*) $t_1/2\pi \in (69, 71.4)$, (*b*) $t_2/2\pi \in (83.4, 85.6)$, (*c*) $t_3/2\pi \in (99, 101.2)$.

procedure, and this was carried out for each value of N. A major result arising from this study is presented in figure 17, which shows how the global maximum growth rate $\beta^{gmax}_{\langle E \text{ or } M \rangle}$ for recurrence varies with the number of waves N in each wave group for each of the densities $\hat{E}_{1/2}$ and $\hat{M}_{1/2}$. This figure highlights two very remarkable results. Most significantly, for both $\hat{E}_{1/2}$ and $\hat{M}_{1/2}$, the global maximum value for recurrence $\beta^{gmax}_{\langle E \text{ or } M \rangle}$ is *insensitive* to N, despite the significant variation of the initial mean carrier

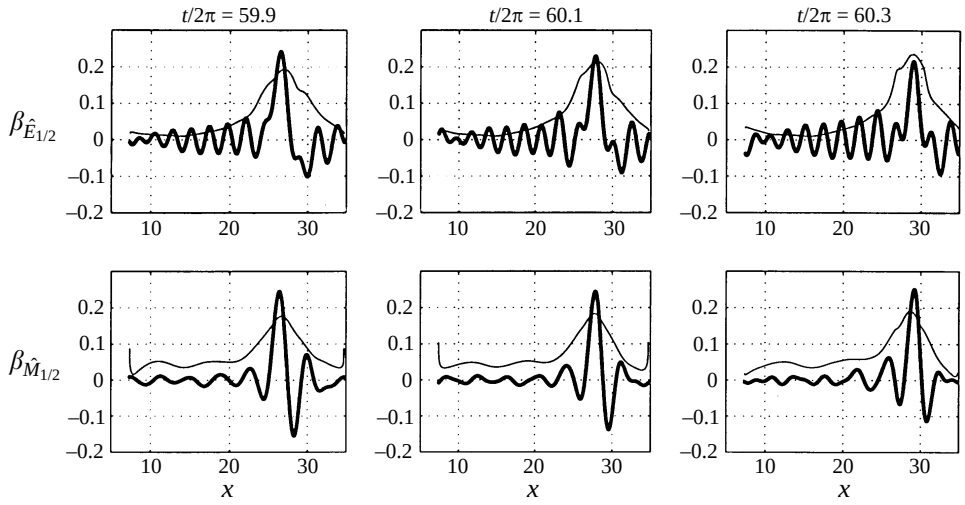

FIGURE 14. Horizontal spatial distribution of β, shown as thick lines, for the breaking case with $(ak)_0 = 0.12$ approaching the onset of breaking. The thin lines are the envelope of the corresponding mean energy or momentum density. Three contiguous times are shown: $t/2\pi = 59.9$, 60.1 and 60.3. Note the relative phase-locking of β^{max} to the envelope maximum compared with the recurrence case shown in figure 12.

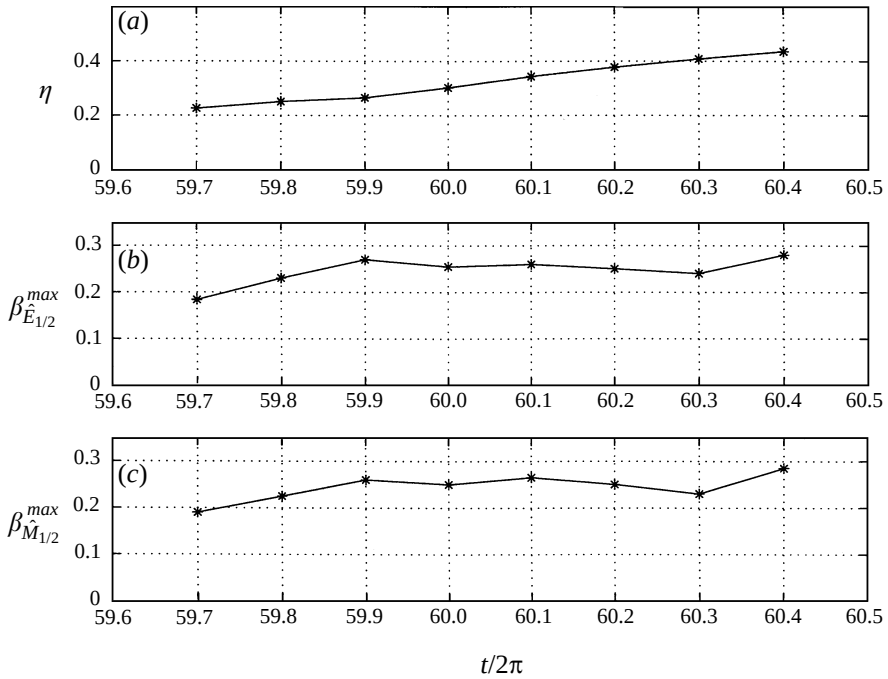

FIGURE 15. As figure 14 but for the temporal evolution of β^{max} during the time interval $t/2\pi \in (59.7, 60.4)$ with breaking occurring at the next time step ($t/2\pi = 60.5$).

wave slope $(ak)_0$ seen in figure 2. It also appears to be insensitive to the initial conditions and to the presence of a uniform vertical shearing current, as discussed below. Figure 17 also shows that cases of $N = 5$ with a different initial wave group configuration and when vertical shear was present are seen to conform closely. These

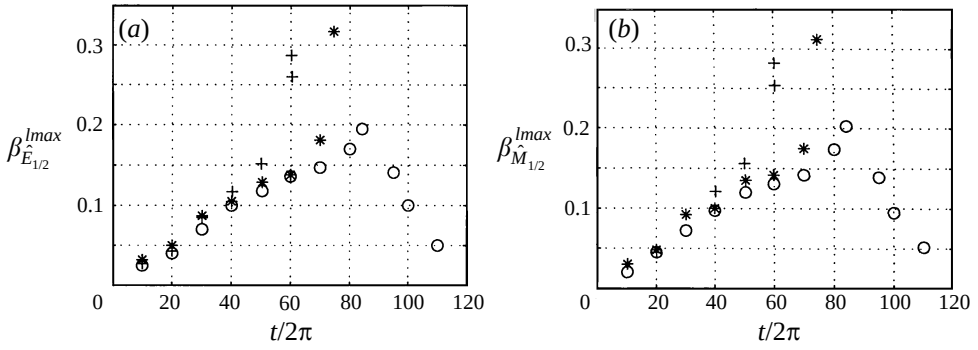

FIGURE 16. Evolution of β^{lmax} for (*a*) $\hat{E}_{1/2}$ and (*b*) $\hat{M}_{1/2}$ for the breaking ($*$) and recurrence ($\bigcirc$) cases shown in figure 1. The case of $(ak)_0 = 0.12$ is shown ($+$).

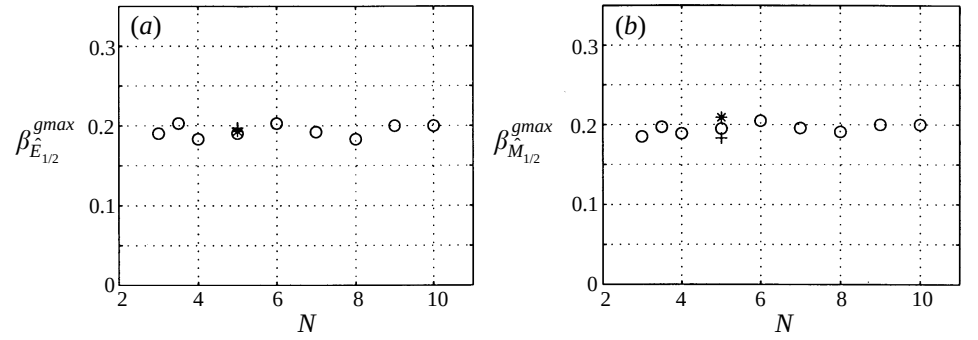

FIGURE 17. The symbols $\bigcirc$ show the variation of β^{gmax}, the global maximum growth rate for recurrence against N, the number of waves in one modulation cycle, for (*a*) $\hat{E}_{1/2}$ and (*b*) $\hat{M}_{1/2}$, for $\Omega = 0$. These results are for the initial wave spectrum (1.1) and the initial steepness values shown in figure 2. The case $\Omega = 0$ with the initial bi-modal spectrum and $\Omega = 0$ described in §3.2.5 is shown ($+$). Also shown with $*$ is the maximal recurrence case of $N = 5$ and $\Omega = 0.2$ documented in figure 19.

cases are described below in §3.2.5 and §3.2.6. Remarkably, the global maximum growth rates for recurrence, $\beta^{gmax}_{\langle E \text{ or } M \rangle}$, are practically identical for $\hat{E}_{1/2}$ and $\hat{M}_{1/2}$, despite the very different nature of the local wave energy and momentum densities. For the ensemble of cases examined, we found a mean value of 0.195 and 0.196 for $\beta^{gmax}_{\langle E \text{ or } M \rangle}$ for $\hat{E}_{1/2}$ and $\hat{M}_{1/2}$ respectively, each with a standard deviation of 0.008. For our present purposes, it suffices to take $\beta^{gmax}_{\langle E \text{ or } M \rangle} = 0.2$.

3.2.4. *The onset of breaking*

In every case of breaking onset, we found two concomitant signatures once the recurrence limit $\beta^{gmax}_{\langle E \text{ or } M \rangle} = 0.2$ was reached. During the ensuing $O(0.5T)$ interval immediately prior to overturning, the growth rate at the envelope maximum, $\beta^{max}_{\langle E \text{ or } M \rangle}$, for both $\hat{E}_{1/2}$ and $\hat{M}_{1/2}$ effectively phase-locks to the envelope (see figure 14), persisting at a large positive ($O(0.2)$) level until the exact moment of overturning (figure 15). This sustained large positive growth rate is the key dynamical factor underlying the onset of breaking. In strong contrast, for all recurrence cases, just beyond the recurrence peak, $\beta^{max}_{\langle E \text{ or } M \rangle}$ rapidly became negative for both $\hat{E}_{1/2}$ and $\hat{M}_{1/2}$, as seen in figure 12.

3.2.5. *Another class of initial wave group structure*

In the past, the wave steepness at breaking has been proposed as an indicator of breaking. It has already been seen in figure 2 that $(ak)_{breaking}$ has a considerable range

of variation with respect to the number of waves in the group for this class of modulating wave train. Mean steepness values observed for breaking waves in the open ocean wave appear to be generally lower than these levels (e.g. Holthuijsen & Herbers 1986). This may be due in part to a difference in the method of measuring this quantity in the field, where it is the post-breaking steepness values that are observed and documented. This motivated investigating other initial modulating wave group configurations that might have lower wave steepness values at breaking. We examined a wave group with an initial bi-modal spectrum of the form $\eta = a\cos(x) + a\cos(1.2x - \pi/18)$. For $N = 5$, we found recurrence for an initial steepness $(ak)_0 = 0.067$, while for $(ak)_0 = 0.070$, breaking occurred for which $(ak)_{breaking}$ was 0.358. This value is very similar to the comparable $N = 5$ case of a wave group with two small symmetric sidebands. Despite the similarity in $(ak)_{breaking}$ values, the onset of breaking occurred considerably earlier – at $t/2\pi = 40$ compared with $t/2\pi = 75$. More significantly, the resulting computations of $\beta^{lmax}_{\langle E \text{ or } M \rangle}$ revealed that the same threshold values $\beta^{gmax}_{\langle E \text{ or } M \rangle}$ were applicable to this case, as shown in figure 17.

3.2.6. *Influence of a uniform surface shear*

The results of Teles da Silva & Peregrine (1988) and Millinazzo & Saffman (1990), amongst others, suggest that a background linear vertical shear current should have a potentially strong influence on the evolution of the wave train. Depending on the strength of the shear, we felt that this might be a contributing factor to the low values of breaking wave steepness observed at sea. This motivated an extension of our study to examine a case of a surface-layer shear current that was typical of well-developed open ocean wave conditions for which wind forcing would be of secondary importance. We note that the actual depth distribution of the surface-layer shear current is a complex research issue, and the interested reader is referred to the recent paper by Craig & Banner (1994) for further details. For the present purpose, we asumed a net surface-layer current of $O(0.03U_{10})$ decreasing linearly over a depth of one significant wave height (SWH). Here, U_{10} is the mean wind speed at the reference height of 10 m above the mean sea level and the SWH is related to the mean energy E of the waves by $\text{SWH} = 4E^{1/2}$. Thus we assumed a shear profile of the form $U(y) = \Omega y$, with $y = 0$ corresponding to mean sea level. The shear rate Ω was estimated using the fully developed Pierson–Moskowitz (1964) wind sea model in which $E = 1.62 \times 10^{-3}\, g^2/(2\pi f_{PM})^4$, where $f_{PM} = 0.13g/U_{10}$. For $U_{10} \sim 10$ m s^{-1}, this yields $\Omega \sim 0.12$ s^{-1}, but to allow for possible underestimation of the surface shear due to the assumed linear shear model, we conducted our detailed investigation using a slightly stronger background shear level of $\Omega = 0.2$ s^{-1} to assess the potential influence of surface-layer shear on the onset of breaking.

After suitable scaling, this background shear was configured within the DP model and the effect of this surface shear layer was investigated for $N = 5$ and the initial wave group specified in §1. The surface shear reduced the steepness at breaking from 0.365 for the shear-free case to 0.306. This point has been included in figure 2. Also, the evolution time to breaking is reduced significantly by the presence of the $\Omega = 0.2$ s^{-1} shear layer. For example, for $N = 5$ and $(ak)_0 = 0.12$, the shear reduces the evolution time to breaking from $t/2\pi = 60.5$ to 47. However, despite the very different value of $(ak)_{breaking}$, the values obtained for $\beta^{gmax}_{\langle E \text{ or } M \rangle}$ were identical to those found in the absence of shear.

Figure 18 illustrates the influence of shear on the evolution in greater detail. Figure 18 compares the evolution of the initial wave group with $N = 5$ and $(ak)_0 = 0.11$ for $\Omega = 0$ (previously shown in figure 16) and $\Omega = 0.2$. It is seen that in the absence of

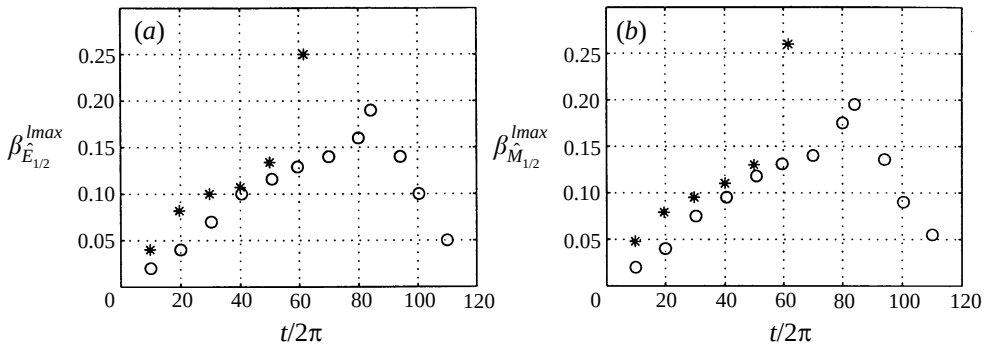

FIGURE 18. Typical examples showing the influence of a background shear on the evolution to breaking of β^{lmax} for (*a*) $\hat{E}_{1/2}$ and (*b*) $\hat{M}_{1/2}$. The initial steepness $(ak)_0 = 0.11$, $N = 5$ and the initial spectrum (1.1): ○ shows the evolution to recurrence for zero background shear ($\Omega = 0$) and ∗ shows that $\Omega = 0.2$ results in evolution to breaking.

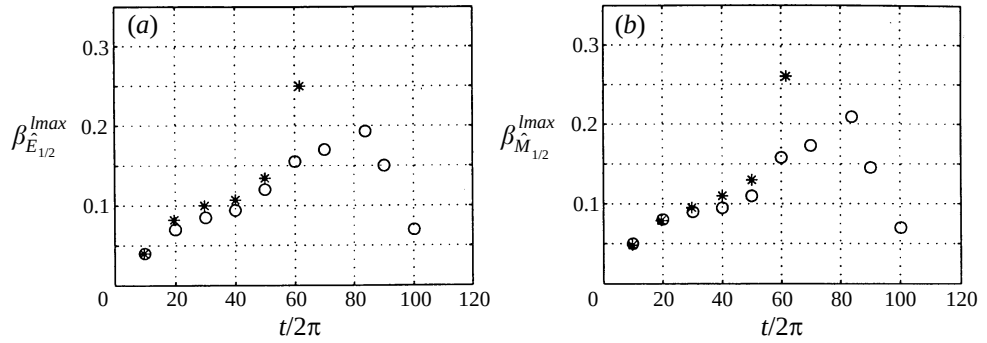

FIGURE 19. As figure 18 but for $\Omega = 0.2$ for $N = 5$: ○ shows the recurrence evolution for initial steepness $(ak)_0 = 0.1025$ and ∗ shows the evolution to breaking that occurs for initial steepness $(ak)_0 = 0.11$. Notice the largest value of β^{lmax} for each of $\hat{E}_{1/2}$ and $\hat{M}_{1/2}$ for the recurrence case with $\Omega = 0.2$ agrees closely with the critical level β^{gmax} for $\Omega = 0$.

shear, recurrence occurs for this initial condition, but when the shear layer is present, instability to breaking now occurs. We determined the marginal stability case for $\Omega = 0.2\ \mathrm{s}^{-1}$ for $N = 5$ and show the evolution curves for $\beta^{lmax}_{\langle E \text{ or } M \rangle}$ for the adjacent recurrence and breaking cases in figure 19. It should be noted that the stability boundary for recurrence now occurs at the lower $(ak)_0$ level of 0.1025. However, the recurrence threshold values for $\beta^{gmax}_{\langle E \text{ or } M \rangle}$ remain at the shear-free levels. These results have been superposed in figure 17.

4. Discussion

Our investigation confirms that the onset of breaking is controlled by the nonlinear behaviour of the wave group and may be determined by the universal threshold $\beta^{gmax}_{\langle E \text{ or } M \rangle}$ proposed here, based on dimensionless growth rates of the local mean energy or momentum densities. These quantities reflect the very complex convergences and divergences of the localized fluxes of momentum and energy within the wave group. Previous efforts to determine the onset of breaking in terms of a local surface variable have not elucidated the underlying wave group dynamics, particularly the crucial time when the recurrence threshold is reached. In the course of this study, we also monitored certain 'traditional' variables such as the wave slope, vertical acceleration at the crest

and horizontal fluid velocity at the crest both at the recurrence peak and at breaking. We did not find universal behaviour in any of these local surface variables, either when the recurrence threshold was reached or at breaking, as we varied the number of waves in the group, added a background shear and varied the initial conditions. However, our study does not exclude the possibility of a *universal* threshold based on another local or a locally averaged surface variable. For the latter, questions arise concerning the underlying dynamical significance and appropriate group velocity, and this is left to a future study. In any event, to be relevant to ocean waves, the study should embrace cases where surface pressure forcing competes with the nonlinear modulation in the presence of vertical shear. We will report on this extension of the investigation in a future paper.

In this study, we searched for possible constraints imposed by the periodic computational domain by examining the case of three wave groups each containing an integer number (3) of carrier waves. This case did not develop any subharmonic instability, reproducing precisely the same behaviour as a single group of three waves with the same initial wave slope specification. As the central wave group was not constrained by the periodicity requirement and was free to deform through nonlinearity, we concluded that the periodicity was not imposing any significant constraints.

The assumption of two-dimensionality is another potential limitation when attempting to extrapolate the present results to the oceanic context. First, documented steepness levels of breaking waves at sea appear to be somewhat lower than the steepness values at breaking determined in our computations (e.g. Holthuijsen & Herbers 1986), but this may be associated with differences in the method of assessing $(ak)_{breaking}$. Our calculated $(ak)_{breaking}$ values were determined at the time step just prior to breaking, while the field observations are based on post-breaking measurements. This difference could be appreciable, depending on the strength of the breaking event and when the steepness was determined during the breaking cycle. This might account for the discrepancy between our results for the background shear case ($(ak)_{breaking} \sim 0.3$) and observed breaker steepness values. Further careful observations that address this issue and distinguish actual dominant wave breaking from parasitic breaking of shorter waves at the crests of the dominant waves are necessary to resolve this aspect. Secondly, according to linear theory, the fastest-growing instabilities of nonlinear wave groups of moderate initial steepness are oblique rather than in the direction of propagation of the wave group (see e.g. Yuen & Lake 1982, §VI, E). Indeed, Melville (1982) observed that for initial wave steepness levels exceeding 0.29, the dominant instabilities were three-dimensional in character. However, extending the computational model to explore these very steep initial wave steepness cases to embrace this aspect is beyond the scope of the present study and left to the future.

5. Conclusions

Determining whether an individual wave will break in an unforced nonlinear modulating wave group has been investigated in terms of the behaviour of non-dimensional relative rates of change of the local mean energy and momentum densities, following their envelopes. The local mean is calculated over one half the local wavelength. The calculations were based on a periodic fully nonlinear two-dimensional inviscid free-surface code used in conjunction with an interior irrotational flow code. Different initial configurations for cases that evolved to breaking revealed a significant range of local wave steepness at the onset of breaking. Cases were included with a

superposed linear background shear typical of ocean surface-layer shear levels, as it was found that the presence of shear significantly reduces the local wave steepness at breaking. The major conclusions of this study are the following.

(*a*) The maxima of the envelopes of the local wave momentum and energy density evolve in a complex fashion, with a fast fluctuation superimposed on a much slower growth or decay. This fast fluctuation is due to our choice of half-wavelength averaging over the strongly asymmetric carrier wave profiles that occur due to nonlinearity. At a critical point in the evolution, either a rapid onset of breaking occurs, or the wave group undergoes a recurrence to close to its initial configuration.

(*b*) Our results provide strong evidence for the existence of a *universal* threshold behaviour of the local relative growth rates of the mean momentum and energy densities that unambiguously differentiates wave groups in which individual steep waves will proceed to break from those that will subsequently undergo recurrence without breaking, once the threshold is reached. Recurrence occurs when the relative growth rates of the mean momentum and energy densities at their envelope maxima reach the threshold of 0.2 and then begin to decrease immediately. In strong contrast, breaking occurs when these relative growth rates are sustained at around this threshold level during the final interval of $O(0.5T)$ just prior to breaking.

As future research on this topic, it remains to verify these two-dimensional results observationally and to account for them in a theoretical framework. While it is known that wave groups of dominant ocean surface waves have intrinsically narrow directionality, typical reported steepness levels of dominant ocean wave breakers appear to be lower than those in our two-dimensional calculations. This may be due to wind influence and/or three-dimensional effects, and it is left to a future study to investigate whether the calculated breaking thresholds in terms of local mean momentum or energy growth rates are modified significantly when these additional factors are involved.

The authors gratefully acknowledge the financial support of the Australian Research Council for this research project. We also sincerely thank our colleagues Professor D. H. Peregrine and Dr J. W. Dold for allowing us to use their free surface code, and Professor J. Fenton and Dr J. Rottman for their helpful technical discussions.

Appendix A. Calculation of interior potential problem

We needed to solve the interior potential problem for a two-dimensional region at any given time for which the unsteady free surface configuration was computed by the DP code. Our numerical scheme for this calculation is described below.

A.1. *Cauchy's integral theorem*

For the two-dimensional irrotational flow field considered here, a complex potential $w = \phi + \mathrm{i}\psi$ exists with ϕ and ψ satisfying Laplace's equation: $\nabla^2\phi = 0$ and $\nabla^2\psi = 0$. The velocity components satisfy the familiar Cauchy–Riemann equations

$$u = \frac{\partial\phi}{\partial x} = \frac{\partial\psi}{\partial y}, \tag{A 1}$$

$$v = \frac{\partial\phi}{\partial y} = -\frac{\partial\psi}{\partial x}. \tag{A 2}$$

When the above relations are satisfied, then the complex function $w = \phi + \mathrm{i}\psi$ has a unique derivative with respect to the complex variable $z = x + \mathrm{i}y$. If $w(z)$ has a

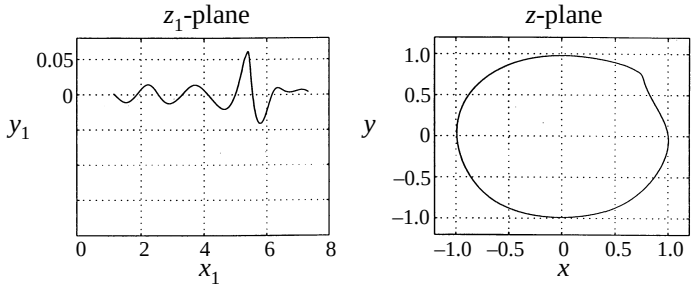

FIGURE 20. Typical example of the conformal mapping $z = \mathrm{e}^{-\mathrm{i}z_1(x_1, y_1)}$. The periodic deep water wave train with $\Omega = 0$, $N = 5$ and $L = 2\pi$ in the z_1-plane is transformed into the closed contour seen in the z-plane.

derivative at each point in the domain, $w(z)$ is analytic. If w is analytic within and on the closed contour C and also if $w(z)$ is known everywhere on the closed contour C, then $w(Z)$ can be calculated at any point Z inside C by Cauchy's integral formula:

$$w(Z) = \frac{1}{2\pi\mathrm{i}} \int \frac{w(z)}{z-Z}\mathrm{d}z. \tag{A 3}$$

Furthermore, equation (A 3) can be written as

$$\int \frac{w(z)-w(Z)}{z-Z}\mathrm{d}z = 0, \tag{A 4}$$

where Z is an interior point within C and z is on the contour C. We note that the integrand in (A 4) is never singular, no matter how closely Z approaches the boundary contour C.

A.2. *A conformal mapping*

In order to apply Cauchy's integral formula, following Fornberg (1980), the infinite fluid surface $Z_1(x_1, y_1)$ in the physical plane is first transformed into a finite closed contour $Z(x, y)$ by the conformal mapping:

$$z(x, y) = \mathrm{e}^{-\mathrm{i}\,(2\pi/\lambda)\, z_1(x_1, y_1)}, \tag{A 5}$$

where λ is the period of the free surface. In the mapped plane Laplace's equation is still satisfied. An example of this conformal mapping is shown in figure 20.

A.3. *Numerical scheme*

We developed a Fortran code based on a simpler and more accurate method exploiting periodicity around the contour as introduced by Fenton (1996). In this approach, a numerical approximation is used to transform the integral equation (A 4) into an algebraic equation by using the trapezoidal rule as follows:

$$\sum_{j=0}^{N-1} \frac{w(z_j)-w(z_k)}{z_j-z_k} z_j' = 0, \tag{A 6}$$

where $z_j' = \mathrm{d}z(j)/\mathrm{d}j$. Here j is a continuous variable that takes on only integer values after the differentiation, and equation (A 6) then holds for each z_j with $j = 0, 1, 2, \ldots, N-1$, at which w is known on the boundary. Also, z_k with $k = 1, 2, \ldots, M$ is the set of M interior points where the flow details are sought.

The geometric coefficient Ω_{kj} is introduced here as

$$\Omega_{kj} = \frac{z_j'}{z_j-z_k}. \tag{A 7}$$

Then the integral equation (A 6) can be written as

$$\sum_{j=0}^{N-1} (w_j - w_k)\,\Omega_{kj} = 0; \tag{A 8}$$

solving for the w_k gives

$$w_k = \frac{\sum_{j=0}^{N-1} w_j\,\Omega_{kj}}{\sum_{j=0}^{N-1} \Omega_{kj}}. \tag{A 9}$$

Clearly, if the value of a complex potential function, say w_j, is known on the boundary and the geometric coefficient above has been calculated, the value of the interior complex potential function w_k can be estimated for any arbitrary point z_k.

As discussed in detail by Fenton (1996), the derivative $z_j' = \mathrm{d}z(j)/\mathrm{d}j$ can be calculated using a Fourier approximation as

$$z_j' = \frac{\mathrm{i}2\pi}{N^2} \sum_{n=1}^{N-1} z_n\, d(j-n), \tag{A 10}$$

where

$$d(j-n) = -\mathrm{i}\frac{N}{2}(-1)^{j-n} \cot(\pi(j-n)\,N) \quad \text{for} \quad j \neq n, \tag{A 11}$$

$$d(0) = 0. \tag{A 12}$$

A.4. *Complex velocity $q = u - \mathrm{i}v$ and its time derivative $q_t = u_t - \mathrm{i}v_t$*

Furthermore, as Laplace's equation is also satisfied for the complex velocity $q = u - \mathrm{i}v$ and its time derivative $q_t = u_t - \mathrm{i}v_t$:

$$\nabla^2 q = 0, \tag{A 13}$$

$$\nabla^2 q_t = 0. \tag{A 14}$$

Therefore, the desired complex velocity and its time derivative for any arbitrary interior point z_k can be calculated as

$$q_k = \frac{\sum_{j=0}^{N-1} q_j\,\Omega_{kj}}{\sum_{j=0}^{N-1} \Omega_{kj}}, \tag{A 15}$$

$$\frac{\partial q_k}{\partial t} = \frac{\sum_{j=0}^{N-1} \frac{\partial q_j}{\partial t}\,\Omega_{kj}}{\sum_{j=0}^{N-1} \Omega_{kj}}. \tag{A 16}$$

Appendix B. The calculation of the derivatives $\mathrm{D}_*\hat{E}/\mathrm{D}t$ and $\mathrm{D}_*\hat{M}/\mathrm{D}t$

As described in §2.4, the derivatives of the mean energy and momentum ($\mathrm{D}_*\hat{E}/\mathrm{D}t$ and $\mathrm{D}_*\hat{M}/\mathrm{D}t$) were used to calculate the growth rates. The expression for the derivative $\mathrm{D}_*/\mathrm{D}t$ was defined as

$$\mathrm{D}_*/\mathrm{D}t = \partial/\partial t + c_{\langle E \text{ or } M\rangle}\,\partial/\partial x. \tag{B 1}$$

That is

$$\mathrm{D}_*\hat{E}/\mathrm{D}t = \partial\hat{E}/\partial t + c_{\hat{E}}\,\partial\hat{E}/\partial x, \tag{B 2}$$

$$\mathrm{D}_*\hat{M}/\mathrm{D}t = \partial\hat{M}/\partial t + c_{\hat{M}}\,\partial\hat{M}/\partial x. \tag{B 3}$$

An outline of the calculations involved is given here for the irrotational and linear shear flow fields investigated in this paper.

B.1. *Wavelength-averaged local mean energy and momentum*

First, we give the forms of the local energy density e and momentum density m, assuming a water density $\rho = 1$. For an irrotational fluid, these can be written as

$$e = \int_{-d}^{\eta} \tfrac{1}{2}(u^2+v^2)\,\mathrm{d}y + \tfrac{1}{2}\eta^2, \tag{B 4}$$

$$m = \int_{-d}^{\eta} u\,\mathrm{d}y. \tag{B 5}$$

In the linear shear case, they become

$$e = e_0 + \frac{\Omega^2}{6}(\eta^3 + d^3), \tag{B 6}$$

$$m = m_0 + \frac{\Omega}{2}(\eta^2 - d^2), \tag{B 7}$$

where e_0 and m_0 are the corresponding local energy and momentum of the irrotational flow component, that is

$$e_0 = \int_{-d}^{\eta} \tfrac{1}{2}(u_0^2+v_0^2)\,\mathrm{d}y + \tfrac{1}{2}\eta^2, \tag{B 8}$$

$$m_0 = \int_{-d}^{\eta} u_0\,\mathrm{d}y, \tag{B 9}$$

and Ω is the magnitude of the constant vorticity of the fluid in the linear shear flow case, $u_0 = u - \Omega y$ is the corresponding irrotational horizontal velocity component of the fluid velocity and $v_0 = v$ is the vertical velocity.

Then, the wavelength-averaged local mean energy density ($\hat{E}$) and momentum density ($\hat{M}$) can be obtained by averaging e and m over one wavelength L (or L is replaced by $L/2$ for half-wavelength averages). The forms for these local mean densities are then

$$\hat{E}(x,t) = L^{-1} \int_{x-L/2}^{x+L/2} e\,\mathrm{d}x', \tag{B 10}$$

$$\hat{M}(x,t) = L^{-1} \int_{x-L/2}^{x+L/2} m\,\mathrm{d}x'. \tag{B 11}$$

For the linear shear flow case, these averaged densities may be written as

$$\hat{E}(x,t) = L^{-1} \int_{x-L/2}^{x+L/2} e_0\,\mathrm{d}x' + L^{-1} \int_{x-L/2}^{x+L/2} \frac{\Omega^2}{6}(\eta^3+d^3)\,\mathrm{d}x', \tag{B 12}$$

$$\hat{M}(x,t) = L^{-1} \int_{x-L/2}^{x+L/2} m_0\,\mathrm{d}x' + L^{-1} \int_{x-L/2}^{x+L/2} \frac{\Omega}{2}(\eta^2-d^2)\,\mathrm{d}x', \tag{B 13}$$

or

$$\hat{E}(x,t) = \hat{E}_0(x,t) + L^{-1} \int_{x-L/2}^{x+L/2} \frac{\Omega^2}{6}(\eta^3+d^3)\,\mathrm{d}x', \tag{B 14}$$

$$\hat{M}(x,t) = \hat{M}_0(x,t) + L^{-1} \int_{x-L/2}^{x+L/2} \frac{\Omega}{2}(\eta^2-d^2)\,\mathrm{d}x', \tag{B 15}$$

where $\hat{E}_0$ and $\hat{M}_0$ are the corresponding wavelength-averaged local mean energy and momentum of the irrotational part of the fluid.

B.2. *Derivatives of $\hat{E}$ and $\hat{M}$*

In order to calculate the growth rates β_E and β_M, the spatial and time derivatives of $\hat{E}$ and $\hat{M}$ were required. The spatial derivatives $\partial\hat{E}/\partial x$ and $\partial\hat{M}/\partial x$ were calculated by a simple first-difference method in the spatial domain. Details of the calculation of the time derivatives $\partial\hat{E}/\partial t$ and $\partial\hat{M}/\partial t$ follow.

For an irrotational flow field, the local time derivatives $\partial e/\partial t$ and $\partial m/\partial t$ are given by

$$\frac{\partial e}{\partial t} = \eta\frac{\partial \eta}{\partial t} + \int_{-d}^{\eta} u\frac{\partial u}{\partial t} + v\frac{\partial v}{\partial t}\,\mathrm{d}y + \frac{\partial \eta}{\partial t}\frac{(u^2(\eta)+v^2(\eta))}{2}, \tag{B 16}$$

$$\frac{\partial m}{\partial t} = \int_{-d}^{\eta} \frac{\partial u}{\partial t}\mathrm{d}y + \frac{\partial \eta}{\partial t}u(\eta), \tag{B 17}$$

where $u(\eta)$ and $v(\eta)$ are the horizontal and vertical velocities on the free surface.

In the linear shear case, the local time derivatives can be written as

$$\frac{\partial e}{\partial t} = \frac{\partial e_0}{\partial t} + \frac{\Omega^2}{2}\,\eta^2\frac{\partial \eta}{\partial t}\,, \tag{B 18}$$

$$\frac{\partial m}{\partial t} = \frac{\partial m_0}{\partial t} + \Omega\eta\frac{\partial \eta}{\partial t}, \tag{B 19}$$

where $\partial e_0/\partial t$ and $\partial m_0/\partial t$ are the local time derivatives of the irrotational flow contributions.

Next we consider the time derivatives of $\hat{E}$ and $\hat{M}$. We note here that in order to avoid calculating $\hat{E}$ and $\hat{M}$ using a difference method at successive time steps, we used the following approximate approach:

$$\frac{\partial \hat{E}}{\partial t} \approx L^{-1}\int_{x-L/2}^{x+L/2}\frac{\partial e}{\partial t}\mathrm{d}x', \tag{B 20}$$

$$\frac{\partial \hat{M}}{\partial t} \approx L^{-1}\int_{x-L/2}^{x+L/2}\frac{\partial m}{\partial t}\mathrm{d}x'. \tag{B 21}$$

The corresponding formulae for the linear shear flow case take the form

$$\frac{\partial \hat{E}}{\partial t} \approx L^{-1}\int_{x-L/2}^{x+L/2}\frac{\partial e_0}{\partial t}\mathrm{d}x' + \frac{\Omega^2}{2}L^{-1}\int_{x-L/2}^{x+L/2}\eta^2\frac{\partial \eta}{\partial t}\mathrm{d}x', \tag{B 22}$$

$$\frac{\partial \hat{M}}{\partial t} \approx L^{-1}\int_{x-L/2}^{x+L/2}\frac{\partial m_0}{\partial t}\mathrm{d}x' + \Omega L^{-1}\int_{x-L/2}^{x+L/2}\eta\frac{\partial \eta}{\partial t}\mathrm{d}x'. \tag{B 23}$$

The accuracy of the above approximations was examined by comparing results using these approximations with typical results for local time derivatives calculated by the finite difference method applied over successive time steps. These tests confirmed that the worst case error was less than 7%.

Appendix C. Properties of the fast fluctuations of the envelopes

The rapid fluctuations detected in the wave envelope maximum and in the associated envelope maxima of $\hat{E}_{1/2}$ and $\hat{M}_{1/2}$ result from the very asymmetric wave profiles that occur successively at the peak of the carrier wave envelope during the evolution. The

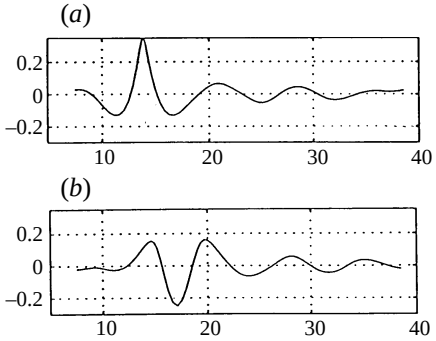

FIGURE 21. The detailed structure of the surface elevation profile at two critical times during the time interval $t/2\pi \in (83.8, 85.8)$ for the recurrence case of $(ak)_0 = 0.11$, $N = 5$, $\Omega = 0$ and the initial spectrum (1.1). These illustrate the strong crest/trough asymmetry due to nonlinearity that is responsible for the first fluctuations in the maximum of the elevation envelope when (*a*) the crest is at the envelope maximum, (*b*) the trough is at the envelope maximum. Figure 11 documents the corresponding variability of the local mean energy and momentum densities.

degree of the crest–trough asymmetry depends on the stage of evolution and is due to the influence of nonlinearity. Figure 21 shows the basis of these fluctuations for the typical case of $N = 5$, $(ak)_0 = 0.11$ and $\Omega = 0$, during the period $t/2\pi \in [83.8, 85.8]$ at the peak of the recurrence cycle when the maximum surface elevation contrast occurs. The maximum value of the envelope elevation is attained when the much sharper and higher crest occupies the envelope maximum, as seen in figure 21(*a*). The minimum value of the envelope maximum is determined by the carrier wave trough elevation, as seen in figure 21(*b*). The difference between these two extremes of the maxima of the elevation envelope over this time interval is seen to be appreciable. This underlies the fast variations in the local mean energy and momentum densities and their relative growth rates reported in the text.

REFERENCES

BANNER, M. L. & PEREGRINE, D. H. 1993 Wave breaking in deep water. *Ann. Rev. Fluid Mech.* **25**, 373–397.

BENJAMIN, T. B. & FEIR, J. E. 1967 The disintegration of wave trains on deep water. *J. Fluid Mech.* **27**, 417–430.

CRAIG, P. J. & BANNER, M. L. 1994 Modelling wave-enhanced turbulence in the ocean surface layer. *J. Phys. Oceanogr.* **24**, 2546–2559.

DOLD, J. W. 1992 An efficient surface-integral algorithm applied to unsteady gravity waves. *J. Comput. Phys.* **103**, 90–115.

DOLD, J. W. & PEREGRINE, D. H. 1986 Water-wave modulation. *Proc. 20th. Intl Conf. Coastal Engng, Taipei*, vol. 1, pp. 163–175. ASCE (referred to herein as DP).

DYSTHE, K. B. 1979 Note on a modification to the nonlinear Schrodinger equation for application to deep water waves. *Proc. R. Soc. Lond.* A **369**, 105–114.

FENTON, J. D. 1996 Exploiting boundary periodicity in the numerical solution of potential problems. In *The Role of Mathematics in Modern Engineering* (ed. A. K. Easton & J. M. Steiner), pp. 565–576. First Biennial Eng. Mathematics Conference, Melbourne, Studentlitteratur, Lund.

FORNBERG, B. 1980 A numerical method for conformal mappings. *SIAM J. Sci. Statist. Comput.* **1**, 385–400.

HAMMACK, J. L. & HENDERSON, D. M. 1993 Resonant interactions among surface water waves. *Ann. Rev. Fluid Mech.* **25**, 55–97.

HARA, T. & MEI, C. C. 1991 Frequency downshift in narrowbanded surface waves under the influence of wind. *J. Fluid Mech.* **230**, 429–477.

Holthuijsen, L. H. & Herbers, T. H. C. 1986 Statistics of breaking waves observed as whitecaps in the open sea. *J. Phys. Oceanogr.* **16**, 290–297.

Lo, E. & Mei, C. C. 1984 A numerical study of water-wave modulation based on a higher order nonlinear Schrodinger equation. *J. Fluid Mech.* **150**, 395–416.

Longuet-Higgins, M. S. & Cleaver, R. J. 1994 Crest instabilities of gravity waves. Part 1. The almost highest wave. *J. Fluid Mech.* **258**, 115–129.

Longuet-Higgins, M. S., Cleaver, R. J. & Fox, M. J. H. 1994 Crest instabilities of gravity waves. Part 2. Matching and asymptotic analysis. *J. Fluid Mech.* **259**, 333–344.

Longuet-Higgins, M. S. & Cokelet, E. D. 1976 The deformation of steep surface waves on water. 1. A numerical method of computation. *Proc. R. Soc. Lond.* A **358**, 1–26.

McLean, J. W. 1982 Instabilities of finite amplitude water waves. *J. Fluid Mech.* **114**, 315–330.

Melville, W. K. 1982 The instability and breaking of deep-water waves. *J. Fluid Mech.* **115**, 165–185.

Melville, W. K. 1983 Wave modulation and breakdown. *J. Fluid Mech.* **128**, 489–506.

Michell, J. H. 1893 The highest waves in water. *Phil. Mag.* **536**, 430–437.

Millinazzo, F. A. & Saffman, P. G. 1990 Effect of surface shear layer on gravity and gravity–capillary waves of permanent form. *J. Fluid Mech.* **216**, 93–101.

Peregrine, D. H. & Thomas, G. P. 1979 Finite amplitude deep water waves on currents. *Phil. Trans. R. Soc. Lond.* A **292**, 371–390.

Phillips, O. M. 1977 *Dynamics of the Upper Ocean*, 2nd Edn. Cambridge University Press.

Pierson, W. J. & Moskowitz, L. 1964 A proposed spectral form for fully developed wind seas based on the similarity theory of S. A. Kitaigorodskii. *J. Geophys. Res.* **69**, 5181–5190.

Rapp, J. R. & Melville, W. K. 1990 Laboratory measurements of deep-water breaking waves. *Phil. Trans. R. Soc. Lond.* A **331**, 735–800.

Schultz, W. W., Huh, J. & Griffin, O. M. 1994 Potential energy in steep and breaking waves. *J. Fluid Mech.* **278**, 201–228.

Skyner, D. 1996 A comparison of numerical predictions and experimental measurements of the internal kinematics of a deep-water plunging wave. *J. Fluid Mech.* **315**, 51–64.

Stokes, G. G. 1847 On the theory of oscillatory waves. *Camb. Phil. Soc. Trans.* **8**, 441–455.

Stokes, G. G. 1880 Considerations relative to the greatest height of oscillatory irrotational waves which can be propagated without change of form. *Math. & Phys. Papers* **1**, 225–228.

Tanaka, M. 1983 The stability of steep gravity waves. *J. Phys. Soc. Japan* **52**, 3047–3055.

Teles Da Silva, A. F. & Peregrine, D. H. 1988 Steep, steady surface waves on water of finite depth with constant vorticity. *J. Fluid Mech.* **195**, 281–302.

Trulsen, K. & Dysthe, K. B. 1990 Frequency downshift through self-modulation and breaking. In *Water Wave Kinematics* (ed. A. Torum & O. T. Gudmestad). Kluwer.

Tulin, M. P. & Li, J. J. 1992 On the breaking of energetic waves. *J. Intl Soc. Offshore and Polar Engng* **2**, 46–53.

Wang, P., Yao, Y. & Tulin, M. P. 1993 Wave group evolution, wave deformation and breaking simulations using LONGTANK, a numerical wave tank. *Proc. Third Intl Offshore and Polar Engng Conf., Singapore*, vol. 27.

Whitham, G. B. 1974 *Linear and Nonlinear Waves*. John Wiley.

Yuen, H. C. & Lake, B. M. 1980 Instabilities of waves on deep water. *Ann. Rev. Fluid Mech.* **12**, 303–334.

Yuen, H. C. & Lake, B. M. 1982 Nonlinear dynamics of deep-water gravity waves. *Adv. Appl. Mech.* **22**, 67–229.

Zaharov, V. E. 1968 Stability of periodic waves of finite amplitude on the surface of a deep liquid. *J. Appl. Mech. Tech. Phys.* **2**, 190–194.